LBL-32435 (Draft)
UC-414

Lawrence Berkeley Laboratory
UNIVERSITY OF CALIFORNIA

Accelerator & Fusion
Research Division

Closed Orbit Distortion and the Beam-Beam Interaction

M. Furman, Y.-H. Chin, J. Eden, W. Kozanecki, J. Tennyson,
and V. Ziemann

June 1992

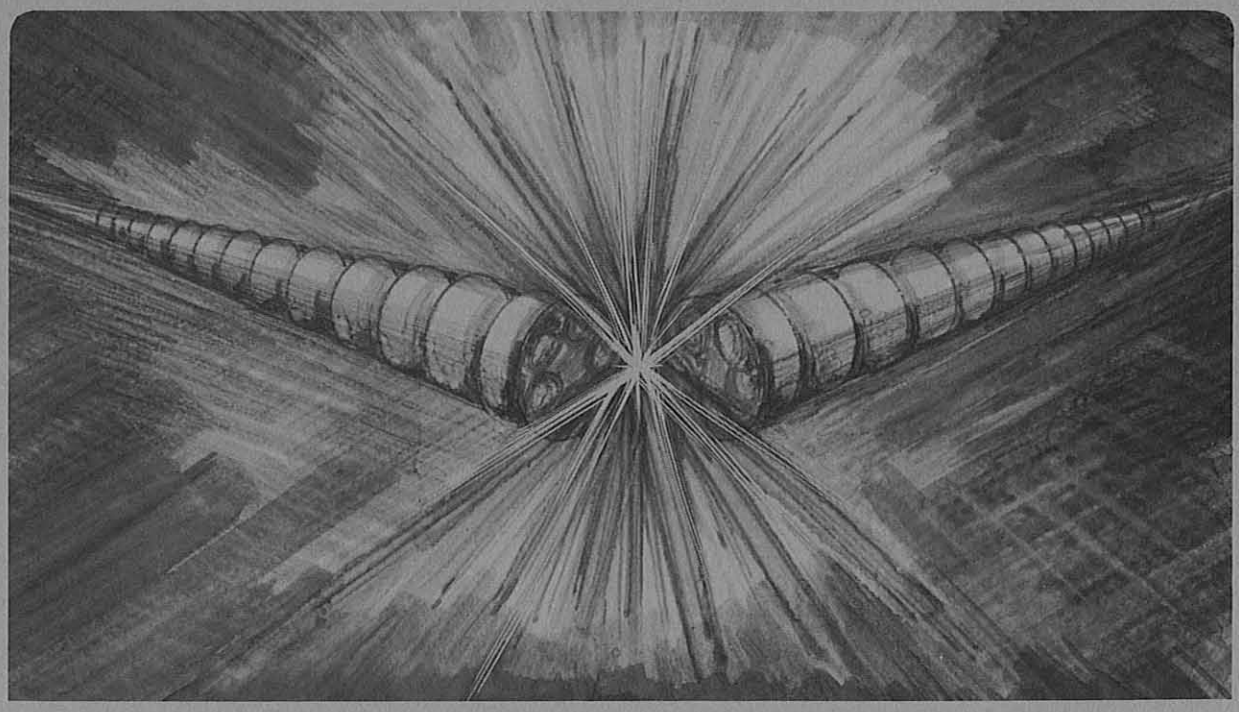

Prepared for the U.S. Department of Energy under Contract Number DE-AC03-76SF00098

DISCLAIMER

LBL–32435, ESG–193, DAPNIA/SPP 92–03, ABC–49

CLOSED ORBIT DISTORTION AND THE BEAM-BEAM INTERACTION*

M. FURMAN, Y.-H. CHIN AND J. EDEN
Lawrence Berkeley Laboratory, Berkeley, CA, USA

W. KOZANECKI
DAPNIA/SPP, CEN-Saclay 91191 Gif-sur-Yvette, France
and
Stanford Linear Accelerator Center, Stanford, CA, USA

J. TENNYSON AND V. ZIEMANN
Stanford Linear Accelerator Center, Stanford, CA, USA

June 1st, 1992

ABSTRACT

We study the applicability of beam-beam deflection techniques as a tuning tool for the SLAC/LBL/LLNL B factory, PEP-II. Assuming that the closed orbits of the two beams are separated vertically at the interaction point by a local orbit bump that is nominally closed, we calculate the residual beam orbit distortions due to the beam-beam interaction. Difference orbit measurements, performed at points conveniently distant from the IP, provide distinct coordinate- or frequency-space signatures that can be used to maintain the beams in collision and perform detailed optical diagnostics at the IP. A proposal to test this method experimentally at the TRISTAN ring is briefly discussed.

* Work supported by the Director of Energy Research, Office of High Energy and Nuclear Physics, High Energy Division, of the U.S. Department of Energy under contracts numbers DE-AC03-76SF00098 and DE-AC03-76SF00515.

Table of Contents

1. Introduction
2. Analytical model for closed-orbit distortions
   2.1 Simplifying assumptions
   2.2 One-turn map
   2.3 Equations for the static dipole mode
   2.4 Limiting expressions for the closed orbit distortion
   2.5 The weak-strong case
   2.6 Consequences of transparency symmetry
   2.7 Spontaneous orbit separation
   2.8 Numerical solution for nominal PEP-II parameters
   2.9 Rule of thumb for the maximum orbit distortion
3. The map in the frequency domain
4. Multiparticle tracking calculations
5. Discussion of experimental feasibility
6. Conclusions

Acknowledgements

References

Figures

1. Introduction

The beam instrumentation needs of the SLAC/LBL/LLNL B Factory (PEP-II) were first considered in the Conceptual Design Report (CDR).[1] Subsequently, possible options for interaction point (IP)-related instruments were reviewed in a one-day workshop.[2] In addition to the traditional synchrotron-light monitors and lifetime-measuring scrapers, this working group studied the feasibility of flying wire scanners,[3] radiative Bhabha luminosity monitors,[4] and the extension of SLC beam-beam techniques to PEP-II. It is this last topic that forms the subject of this paper.

Because of their two-ring structure, asymmetric B factories share, in a sense, some of the basic features of both circular and linear colliders. Single-beam dynamics follows the same basic rules as in conventional storage rings. In particular, the combination of the closed orbit constraint and of radiation damping provides a

natural stabilization mechanism that is missing in linear colliders, where each pulse must be mastered anew. On the other hand, because the two beams do not follow identical orbits, central collisions are not guaranteed and must be maintained by active feedback. This independence of the two beams (except for the beam-beam interaction) allows one to envisage beam diagnostics that are fundamentally inapplicable to a single-ring e^+–e^- collider, but have proved very powerful at the SLC.

The most obvious such case is that of beam-beam deflections, induced by one beam on the other via the dipole mode of the beam-beam interaction.[5] At the SLC, this deflection supplies an intense and unambiguous signal in beam position monitors that is used routinely to maintain beams in collision.[6] This technique also constitutes the backbone of a complete optical tuning procedure by which the beam matrix at the IP can be experimentally diagonalized and the luminosity optimized.[7]

Transplanting these techniques to an asymmetric collider raises fundamental questions: What is the impact of large beam-beam dipole kicks on the closed orbit? How do the beam-beam effects, so important in this machine, modify the naive model of single-pass, impulse-approximation, rigid beam collisions that is applicable at the SLC? Can beam blowup, in the case of off-axis collisions, sufficiently distort the beam shape or the beam lifetime to render the approach impractical?

This report is organized as follows: In Sec. 2 we study the effect on the closed orbit of deliberately off-centering the beams at the IP, under the simplifying assumptions (Sec. 2.1) of rigid Gaussian beams acting on each other as thin lenses. Such an analysis allows an exact mathematical solution[8] (Sec. 2.2, 2.3) which reveals (Sec. 2.4, 2.5) fundamental features of the phenomena studied, such as effects of transparency symmetry (Sec. 2.6) or spontaneous orbit separation (Sec. 2.7). The period-one fixed point condition for the one-turn map provides an elegant numerical solution (Sec. 2.8) for the residual closed orbit distortion, which establishes, at least in the rigid-beam, thin-lens case, the viability of the beam deflection technique. The well-known signature of the dipole beam-beam interaction in the frequency domain is examined in Sec. 3, under the same assumptions as those of Sec. 2. In Sec. 4 we relax most of our assumptions and study the closed-orbit distortion for beams colliding off-center, by means of "strong-strong" multiparticle tracking simulations that take into account synchrotron motion, noise, radiation damping, thick lens effects and beam blowup. The experimental feasibility of using beam-beam-induced orbit distortions as an orbital and optical diagnostic tool is evaluated in Sec. 5, in the context of a proposed experiment at TRISTAN. Our conclusions are collected in Sec. 6.

In the interest of simplicity of the analysis, we neglect in this paper all effects

from parasitic crossings. It is a straightforward matter to include these effects in multiparticle simulations; we shall do so in a future note.

2. Analytical model for closed-orbit distortions

Under the simplifying assumptions listed below we can carry out the analytical calculation of the closed orbit at any point in the ring. (Because of these assumptions, this calculation is of limited accuracy; nevertheless, it exhibits the general qualitative features of the closed orbit distortion and its dependence on parameters such as the tune, the beam-beam parameter and the azimuthal position of the observation point). For typical PEP-II parameters the result of this calculation is in good qualitative agreement with multiparticle tracking simulations (Sec. 4) that do not involve these assumptions.

The analysis presented here follows that of Hirata and Keil,[8] suitably augmented to include a closed orbit bump at the interaction point (IP). Our presentation is deliberately quite explicit in the hope that this study will be useful in further analyses or in B-factory-related experiments.

2.1. Simplifying assumptions

We assume that there exists a closed orbit bump that splits the closed orbits apart vertically by a distance d in the immediate neighborhood of the IP. For our purposes, it does not matter how this distance is apportioned between the e^+ and the e^- beams as long as the total separation of the nominal orbits adds up to d. In the context of this note, this orbit bump is a calculational device that provides a convenient variable to test the sensitivity of the closed orbit to the beam-beam force. In practice, such a bump would be intentionally implemented with appropriate magnets or electrostatic beam separators. We assume that this orbit bump is nominally closed, *i.e.*, that in the absence of the beam-beam force the orbits coincide exactly with the nominal orbits in the region "outside" the bump. Because of the beam-beam interaction, however, there is a residual closed orbit distortion everywhere in the ring. The situation is sketched in Fig. 1. The basic objective in this note is to compute this residual orbit distortion as a function of d and other parameters.

For the purposes of this section we make the following assumptions:

(a) The orbit bump is nominally closed, and exists only in the immediate neighborhood of the IP. The orbits are parallel-displaced by a distance d in the vertical direction only.

(b) The bunches are not tilted.

(*c*) All effects of any parasitic crossings are ignored.

(*d*) The beam sizes are independent of d and have their nominal values.

(*e*) The beam-beam interaction is treated in the impulse (thin-lens) approximation.

(*f*) For the purpose of computing the beam-beam kick, the particle distributions are assumed Gaussian.

The analytical calculation presented in this section addresses only the coupled dipole mode of the beams (rigid-Gaussian approximation). This calculation can be easily extended to the case in which the orbits are displaced in an arbitrary direction rather than vertically, and in which the beams are tilted in the transverse plane.[9] We do not consider these generalizations in this note.

We will remove assumptions (*d*) and (*e*) in Sec. 4 by resorting to strong-strong multiparticle tracking simulations, in which the beam sizes are determined dynamically and the beam-beam collision is treated in the thick-lens approximation. Assumptions (*c*) and (*f*), however, will remain in force even then. An extension of these simulations to include parasitic crossing collisions is straightforward and will be presented separately. The importance of allowing for a self-consistent treatment of non-Gaussian particle distributions has been recently emphasized;[10] an extension of our calculation along these lines remains to be investigated.

2.2. One-turn map

We assume that the two rings are represented by linear maps. The rings intersect at the IP, which we choose to be the origin for the azimuthal coordinate s for both rings. We imagine observing the beams at every turn at a point immediately before the IP. The resultant map that relates turn n to turn $n+1$ for *an individual particle* at this surface of section is written

$$\begin{bmatrix} x_\pm \\ x'_\pm \\ y_\pm \\ y'_\pm \end{bmatrix}_{n+1} = \begin{bmatrix} M_{x\pm} & 0 \\ & \\ 0 & M_{y\pm} \end{bmatrix} \begin{bmatrix} x_\pm \\ x'_\pm + \Delta x'_\pm \\ y_\pm \\ y'_\pm + \Delta y'_\pm \end{bmatrix}_n . \tag{2.1}$$

where $+$ and $-$ label the positron and electron beams, respectively. The coordinates x, y and slopes x', y' are measured relative to the nominal closed orbits. The M's are the usual Courant-Snyder matrices

$$M_{x\pm} = \begin{pmatrix} \cos(2\pi\nu_{x\pm}) + \alpha^*_{x\pm}\sin(2\pi\nu_{x\pm}) & \beta^*_{x\pm}\sin(2\pi\nu_{x\pm}) \\ -\gamma^*_{x\pm}\sin(2\pi\nu_{x\pm}) & \cos(2\pi\nu_{x\pm}) - \alpha^*_{x\pm}\sin(2\pi\nu_{x\pm}) \end{pmatrix} \tag{2.2}$$

with a corresponding expression for $M_{y\pm}$. Here α, β and γ are the usual lattice functions, satisfying $\beta\gamma = 1 + \alpha^2$, and the superscript $*$ refers to the IP ($s = 0$). As is customary, the design is such that $\alpha^*_{x\pm} = \alpha^*_{y\pm} = 0$.

$\Delta x'$ and $\Delta y'$ describe the deflection produced by the opposing bunch as a result of the beam-beam kick. The deflection that *an individual positron* at position $\mathbf{x}_+$ suffers in the collision is given, in complex form, in the impulse approximation, and in the relativistic limit by

$$\Delta x'_+ + i\Delta y'_+ = -\frac{r_0 N_-}{\gamma_+} F(\mathbf{x}_+ - \mathbf{X}_-, \sigma_{x-}, \sigma_{y-}) \tag{2.3}$$

(a corresponding expression applies to an electron in the opposing bunch, obtained by exchanging $+ \leftrightarrow -$). Here $r_0 \equiv e^2/mc^2 \simeq 2.815 \times 10^{-15}$ m is the classical electron radius, N_- is the number of particles in the electron bunch, $\mathbf{X}_- = (X_-, Y_-)$ is the position of its centroid relative to the nominal orbit, and σ_{x-}, σ_{y-} are its rms beam sizes at the collision point. γ_+ is the usual relativistic factor of the positron and F is a complex function* that, for Gaussian distributions, is expressed in terms of the complex error function.[11]

The one-turn map, Eq. (2.1), is averaged over the particle distributions to yield a map for the centroids. The centroid is defined by the simple particle average

$$(X, Y) \equiv \frac{1}{N} \sum_{k=1}^{N} (x_k, y_k) \tag{2.4}$$

As a consequence of the thin-lens approximation (bunch length is effectively zero), the resultant map for the centroids is of the same form as the individual-particle map,

$$\begin{bmatrix} X_\pm \\ X'_\pm \\ Y_\pm \\ Y'_\pm \end{bmatrix}_{n+1} = \begin{bmatrix} M_{x\pm} & 0 \\ & \\ 0 & M_{y\pm} \end{bmatrix} \begin{bmatrix} X_\pm \\ X'_\pm + \Delta X'_\pm \\ Y_\pm \\ Y'_\pm + \Delta Y'_\pm \end{bmatrix}_n \tag{2.5}$$

The deflection of the centroid of the positron bunch is obtained by averaging both sides of Eq. (2.3) over the positron bunch distribution, assumed Gaussian,

---

* Our definition of F differs from that in Ref. 11 by complex conjugation and a factor of $2i$.

and the result is[12]

$$\Delta X'_+ + i\Delta Y'_+ = -\frac{r_0 N_-}{\gamma_+} F(\mathbf{X}_+ - \mathbf{X}_-, \Sigma_x, \Sigma_y) \tag{2.6}$$

where

$$\Sigma_x = \sqrt{\sigma_{x+}^2 + \sigma_{x-}^2}, \qquad \Sigma_y = \sqrt{\sigma_{y+}^2 + \sigma_{y-}^2} \tag{2.7}$$

A similar expression applies to the electron beam, obtained from the above by the replacement $+ \leftrightarrow -$. The fact that the same function F appears in both Eqs. (2.3) and (2.6), albeit with different arguments, is a property peculiar to the Gaussian distribution. This mathematical property certainly makes it advantageous to use this distribution in the analysis of the problem; it should be remembered, however, that, in practice, the beam shape is only approximately Gaussian. Also, under certain operating conditions, the distributions can differ substantially from Gaussian.

Eqs. (2.5) and (2.6) fully describe the one-turn map for the centroids of the two beams for given rms beam sizes (in practice, the beam sizes change turn by turn until an equilibrium is reached). We have not included radiation damping and quantum excitation because they are not important in determining the closed orbit: they are important in determining the *approach* to the equilibrium orbit, but not the orbit itself. Radiation damping and quantum excitation are much more important for the quadrupole and higher modes, and therefore these effects are fully included in the multiparticle simulations used in Sec. 4.

2.3. Equations for the static dipole mode

The above map determines the dynamics of the centroids, or the dipole motion, of the beams, within our approximations. We first look for a period-one fixed point of the map. If this static solution exists and is stable we call it, by definition, the closed orbit. The defining condition is $\langle \cdots \rangle_{n+1} = \langle \cdots \rangle_n$, where $\cdots$ represents the centroids and the sizes of either beam.

In our particular case, in which the displacement of the orbits produced by the bump is purely vertical, we look for static solutions with $X_+ = X_- = 0$. The function F is nothing but the electric field (in complex from) per unit charge produced by the particle distribution in the $x - y$ plane. Because the Gaussian distribution is an even function of x and y, F is odd in x and y. Therefore the condition $X_+ = X_- = 0$ implies that $\Delta X'_+ = \Delta X'_- = 0$, which means that the static solution for the horizontal map is the trivial one (this is not true if the condition for "spontaneous orbit separation" is satisfied; see below.)

Referring to Fig. 1, in which we define the vertical components of the centroids Y_+ and Y_- measured *from their respective closed orbits*, one sees that the actual separation between the orbits is $Y_+ - Y_- + d$. We obtain from (2.6)

$$\begin{aligned} \Delta Y'_+ &= -\frac{r_0 N_-}{\gamma_+} \mathrm{Im}F(0, Y_+ - Y_- + d, \Sigma_x, \Sigma_y) \\ \Delta Y'_- &= -\frac{r_0 N_+}{\gamma_-} \mathrm{Im}F(0, Y_- - Y_+ - d, \Sigma_x, \Sigma_y) \end{aligned} \tag{2.8}$$

From Eq. (2.5) one easily finds the well-known solution[13] for the period-1 fixed point

$$Y_\pm = \tfrac{1}{2} \Delta Y'_\pm \beta^*_{y\pm} \cot(\pi \nu_{y\pm}) \tag{2.9}$$

which, when combined with Eq. (2.8), yields a set of two nonlinear equations for the two unknowns Y_+ and Y_-,

$$\begin{aligned} Y_+ &= -\frac{r_0 N_- \beta^*_{y+}}{2\gamma_+} \cot(\pi \nu_{y+}) \, \mathrm{Im}F(0, Y_+ - Y_- + d, \Sigma_x, \Sigma_y) \\ Y_- &= -\frac{r_0 N_+ \beta^*_{y-}}{2\gamma_-} \cot(\pi \nu_{y-}) \, \mathrm{Im}F(0, Y_- - Y_+ - d, \Sigma_x, \Sigma_y) \end{aligned} \tag{2.10}$$

This set can be solved by first reducing it to a single equation for $Y_+ - Y_-$ by subtracting the two equations. Thus one finds, using the antisymmetry of $\mathrm{Im}F$,

$$z = (A_{y+} + A_{y-}) \; \mathrm{Im}F(0, z + d, \Sigma_x, \Sigma_y) \tag{2.11}$$

where $z = Y_+ - Y_-$ and

$$A_{y+} = -\frac{r_0 N_- \beta^*_{y+}}{2\gamma_+} \cot(\pi \nu_{y+}), \qquad A_{y-} = -\frac{r_0 N_+ \beta^*_{y-}}{2\gamma_-} \cot(\pi \nu_{y-}) \tag{2.12}$$

Once a solution is found for z, the beam offsets Y_+ and Y_- are obtained by plugging z into the right-hand side of Eqs. (2.10).

Under the assumption that $\alpha^*_{y\pm} = 0$, Eq. (2.5) also implies that the period-1 fixed point satisfies

$$\Delta Y'_\pm = -2Y'_\pm \tag{2.13}$$

which means that the slopes of the closed orbit immediately before and immediately after the IP are equal and opposite.

If both tunes $\nu_{y\pm}$ are below the half-integer the cotangent term is positive and Eq. (2.11) implies that the orbits "attract" each other (the actual separation is $< d$). If the tunes are above the half-integer, the opposite is true and the orbits "repel" each other. The equation also implies that the closed orbit offset vanishes for $\nu_{y\pm} = n + 1/2$. This is misleading: although the period-1 fixed point solution does vanish, it turns out that it is unstable, and the period-2 fixed point solution is divergent for half-integer tunes.[8]

The solution to the set of equations (2.10) is discussed analytically and numerically in the following subsections. The closed orbit displacement at any point s in the ring is determined by applying the usual transport matrix; the result is

$$\begin{aligned} Y_\pm(s) &= \frac{\Delta Y'_\pm}{2\sin(\pi\nu_{y\pm})}\sqrt{\beta^*_{y\pm}\beta_{y\pm}(s)}\cos(\phi_{y\pm}(s) - \pi\nu_{y\pm}) \\ &= Y_\pm(0)\sqrt{\frac{\beta_{y\pm}(s)}{\beta^*_{y\pm}}}\,\frac{\cos(\phi_{y\pm}(s) - \pi\nu_{y\pm})}{\cos(\pi\nu_{y\pm})} \end{aligned} \tag{2.14}$$

where $Y_\pm(0)$ is what we have heretofore called $Y_\pm$, and $\phi_{y\pm}(s)$ is the betatron phase advance measured from the IP.

This equation implies that, in an idealized ring, a measurement of the closed orbit $Y_\pm(s)$ allows one, in principle, to determine the closed orbit offset at the IP. This diagnostic might be input to a feedback system in order to optimize the collisions. In practice one might choose not one but many observation points s; for example, one might measure the orbit at all beam position monitors, typically near the center of all quadrupole magnets. We will briefly discuss such a scheme in Sec. 5. For present purposes, we shall limit ourselves to finding $Y_\pm$ and $\Delta Y'_\pm$.

It is worth noting that transverse momentum conservation during the collision implies the easily-proven equality

$$\gamma_+ N_+ \Delta Y'_+ + \gamma_- N_- \Delta Y'_- = 0 \tag{2.15}$$

with a corresponding equation for the horizontal deflections. This equality is satisfied turn by turn, whether or not the dynamics has reached a fixed point. In particular, Eqs. (2.8) for the period-1 fixed point do satisy this general property.

2.4. Limiting expressions for the closed orbit distortion

As mentioned earlier, for the case of Gaussian charge distribution, F is expressed in terms of the complex error function.[11] The leading terms at short and long distance are given by

$$F(x,y,\sigma_x,\sigma_y) = \begin{cases} \dfrac{2}{\sigma_x+\sigma_y}\left(\dfrac{x}{\sigma_x}+i\dfrac{y}{\sigma_y}\right)+\cdots, & \text{if } 0 \le \left|\dfrac{x}{\sigma_x}+i\dfrac{y}{\sigma_y}\right| \lesssim 1 \\ \dfrac{2}{x-iy}+\cdots, & \text{if } \left|\dfrac{x}{\sigma_x}+i\dfrac{y}{\sigma_y}\right| \gg 1 \end{cases} \tag{2.16}$$

By using these expressions one can find, analytically, the limits of the solution for small d and for large d in the case when the beam-beam interaction is sufficiently weak that there is no spontaneous orbit separation. This condition is satisfied in the APIARY 7.5 design of PEP-II, and almost certainly in the design of all other existing or planned colliders (see below for a detailed discussion of spontaneous orbit separation). By inserting the first approximation for F into the closed-orbit equations (2.10) we find, to first order in d,

$$Y_\pm = \mp 2\pi \Xi_{y\pm}\, d \cot(\pi\nu_{y\pm}) + \mathcal{O}(d^2), \qquad \Delta Y'_\pm = \mp 4\pi \Xi_{y\pm} \frac{d}{\beta^*_{y\pm}} + \mathcal{O}(d^2) \tag{2.17}$$

where Ξ_{y+} is one of the four coherent beam-beam parameters, defined by[8]

$$\Xi_{y+} = \frac{r_0 N_- \beta^*_{y+}}{2\pi\gamma_+ \Sigma_y(\Sigma_x+\Sigma_y)} \tag{2.18}$$

with corresponding expressions for the remaining three, obtained by the exchanges $+ \leftrightarrow -$ and $x \leftrightarrow y$. Expression (2.17) shows that the effective strength of the dipole mode of the beam-beam interaction for small separations is $\propto \Xi \cot(\pi\nu)$ rather than $\propto \xi$ (ξ = the usual incoherent beam-beam parameter).

In the limit of large separation the beam-beam force decreases as the electric field falls off as $2/r$, as seen in the large-distance approximation for F. In this case we obtain, for $d \gg \Sigma_x,\ \Sigma_y$,

$$Y_\pm = \mp \frac{r_0 N_\mp \beta^*_{y\pm}}{\gamma_\pm d} \cot(\pi\nu_{y\pm}) + \mathcal{O}(d^{-2}), \qquad \Delta Y'_\pm = \mp \frac{2 r_0 N_\mp}{\gamma_\pm d} + \mathcal{O}(d^{-2}) \tag{2.19}$$

2.5. THE WEAK-STRONG CASE

If one of the beams contains much fewer particles than the other one, we call it the "weak beam" (this is not the only definition of "weak beam" used in the literature). We consider the extreme case in which the weak beam is a single particle, say a positron. Thus we take the limit $N_+,\ \sigma_{x+},\ \sigma_{y+} \to 0$ with $N_-,\ \sigma_{x-},\ \sigma_{y-}$ fixed. Eqs. (2.10) yields $Y_- = \Delta Y'_- = 0$, which means that the orbit of the strong beam is not disturbed, as it should be expected. On the other hand, the equation for the orbit offset of the weak beam becomes

$$Y_+ = A_{y+}\,\mathrm{Im}F(0, Y_+ + d, \sigma_{x-}, \sigma_{y-}) \tag{2.20}$$

which is quite similar to Eq. (2.11). In the limit of small d the solution is

$$Y_+ = -2\pi\xi_{y+}\,d\cot(\pi\nu_{y+}) + \mathcal{O}(d^2), \qquad \Delta Y'_+ = -4\pi\xi_{y+}\,\frac{d}{\beta^*_{y+}} + \mathcal{O}(d^2) \tag{2.21}$$

where ξ_{y+} is one of the four incoherent beam-beam parameters, defined by

$$\xi_{y+} = \frac{r_0 N_- \beta^*_{y+}}{2\pi\gamma_+\sigma_{y-}(\sigma_{x-} + \sigma_{y-})} \tag{2.22}$$

with corresponding expressions for the remaining three, obtained by the exchanges $+ \leftrightarrow -$ and $x \leftrightarrow y$.

In the case $d \gg \sigma_{x-},\ \sigma_{y-}$ we obtain

$$Y_+ = -\frac{r_0 N_- \beta^*_{y+}}{\gamma_+ d}\cot(\pi\nu_{y+}) + \mathcal{O}(d^{-2}), \qquad \Delta Y'_+ = -\frac{2r_0 N_-}{\gamma_+ d} + \mathcal{O}(d^{-2}) \tag{2.23}$$

which are identical to the strong-strong results, Eq. (2.19). The reason that the weak-strong and strong-strong results are the same at large distance is that the beams behave, in leading order, like point particles in this limit.

This weak-strong case is of interest because it provides a first check on a tracking program when it is used to calculate the orbit offset. In Sec. 2.8 we compare the solution of Eq. (2.20) with that of such a program for the case of the APIARY 7.5 design of PEP-II.

2.6. Consequences of transparency symmetry

In the present conception[1] of the PEP-II B factory the nominal parameters satisfy a transparency symmetry[14] whose relevant ingredients can be stated, for our purposes, as:

$$\begin{aligned} \frac{N_-\beta^*_{y+}}{\gamma_+} &= \frac{N_+\beta^*_{y-}}{\gamma_-} \\ \sigma_{x+} = \sigma_{x-} \qquad & \sigma_{y+} = \sigma_{y-} \\ \nu_{x+} = \nu_{x-} \qquad & \nu_{y+} = \nu_{y-} \end{aligned} \tag{2.24}$$

In this case it is easy to see that the two equations in (2.10) are identical, except for an overall sign; therefore the orbit offsets of the two beams are very simply related by

$$Y_+ = -Y_- , \qquad \frac{\Delta Y'_+}{\Delta Y'_-} = -\frac{\beta^*_{y-}}{\beta^*_{y+}} \tag{2.25}$$

It is worth remarking that the second equality in (2.25), satisfied by the deflections $\Delta Y'_\pm$, is valid turn by turn, whether the dynamics has or has not reached a fixed point. The reason that this equality is more generally valid than what our derivation would imply is that it follows from transverse momentum conservation, Eq. (2.15), combined with the first transparency-symmetry condition in (2.24). On the other hand, the first equality in (2.25), satisfied by the offsets $Y_\pm$, is valid only at the period-1 fixed point in the transparent-symmetric case.

2.7. Spontaneous orbit separation

Consider now the case in which there is no orbit bump, *i.e.*, $d = 0$. Then Eq. (2.11) has the obvious solution $z = 0$, which implies $Y_+ = Y_- = 0$. This is the "normal" solution, in which the closed orbits coincide with the nominal orbits despite the beam-beam interaction. However, if the beam-beam interaction is effectively strong, this solution is not unique and, in fact, not stable.[8] There is a critical value of the strength of the beam-beam interaction beyond which two new, nonzero, symmetric, solutions for z appear in Eq. (2.11). By studying the one-turn map one can show that these solutions are, in fact, the stable ones; the system chooses one or the other depending on the initial conditions. This implies that Y_+ and Y_- are nonzero despite the fact that $d = 0$. This undesirable solution corresponds to "spontaneous orbit separation of the first kind," and is analogous to the spontaneous magnetization of a ferromagnet below the Curie temperature. It can be shown that it occurs when the derivative with respect to z of the right-hand side of Eq. (2.11) is greater than unity at $z = 0$. From Eq. (2.16) and the definition

(2.18) one finds that the necessary and sufficient condition for the occurrence of spontaneous orbit separation is

$$-2\pi\Big(\Xi_{y+}\cot(\pi\nu_{y+})+\Xi_{y-}\cot(\pi\nu_{y-})\Big)>1 \tag{2.26}$$

Because the beam-beam parameters are positive, this condition requires at least one of the tunes to be above the half-integer, where the cotangent is negative. For given $\Xi_{y\pm}$, the condition is always satisfied if at least one of the tunes $\nu_{y\pm}$ is below and sufficiently close to an integer.

Also possible is a "spontaneous orbit separation of the second kind." In this case the solution for the fixed point of the map has period two, so that the closed orbits of the beams alternate from turn to turn between the two nonzero solutions of Eq. (2.11). The necessary and sufficient condition for the occurrence of this undesirable solution is[8]

$$2\pi\Big(\Xi_{y+}\tan(\pi\nu_{y+})+\Xi_{y-}\tan(\pi\nu_{y-})\Big)>1 \tag{2.27}$$

which is satisfied if at least one of the tunes $\nu_{y\pm}$ is below and sufficiently close to a half-integer.

For the APIARY 7.5 design each of the four nominal coherent beam-beam parameters satisfies

$$\Xi=\tfrac{1}{2}\xi \tag{2.28}$$

as a consequence of the pairwise equality of the nominal rms beam sizes. Furthermore, transparency symmetry implies $\xi_{y+}=\xi_{y-}$ and $\nu_{y+}=\nu_{y-}$. Thus the condition for spontaneous orbit separation of the first kind becomes

$$\xi_y>-\tfrac{1}{2\pi}\tan(\pi\nu_y) \qquad \text{for } 1>\nu_y>0.5 \tag{2.29}$$

while the condition for spontaneous orbit separation of the second kind is

$$\xi_y>\tfrac{1}{2\pi}\cot(\pi\nu_y) \qquad \text{for } 0>\nu_y>0.5 \tag{2.30}$$

These two conditions define undesirable regions in the $\xi-\nu$ plane shown shaded in Fig. 2. The APIARY 7.5 design avoids these regions comfortably.

Hirata and Keil[8] also point out that asymmetric colliders can have a third kind of instability corresponding to a sum resonance. The instability occurs when

$$\nu_{y+}+\nu_{y-}\lesssim \text{ integer} \tag{2.31}$$

which is also avoided by the APIARY 7.5 design.

2.8. Numerical solution for nominal PEP-II parameters

Eq. (2.11) can be easily solved by iteration in most cases of practical interest. Here we present the solution for the case of nominal PEP-II parameters.* A list with approximate values for the parameters is presented in Table 1. The actual values that were used as input in the various calculations throughout this paper vary slightly from those in this table, and are displayed in full at the right margin of each figure.

Table 1. Abbreviated list of APIARY 7.5 parameters.

	LER (e^+)	HER (e^-)
E [GeV]	3.1	9.0
N	5.6×10^{10}	3.9×10^{10}
β_x^* [cm]	37.5	75.0
β_y^* [cm]	1.5	3.0
σ_{0x}^* [μm]	186	186
σ_{0y}^* [μm]	7.4	7.4
$\sigma_{0x}'^*$ [mrad]	0.5	0.25
$\sigma_{0y}'^*$ [mrad]	0.5	0.25
σ_ℓ [cm]	1.0	1.0
σ_E/E	1.0×10^{-3}	6.1×10^{-4}
ν_s	0.04	0.05
τ_x [turns]	5×10^3	5×10^3
τ_y [turns]	5×10^3	5×10^3
τ_ℓ [turns]	2.5×10^3	2.5×10^3
ν_x	0.64	0.64
ν_y	0.57	0.57

In this table the rms beam sizes σ^* and rms angular divergences σ'^* at the IP carry a subscript 0 to emphasize that these are nominal values, corresponding to completely neglecting the effects of the beam-beam interaction. As mentioned earlier, the calculation of this section assumes rigid bunches whose rms sizes are fixed at their nominal values.

* Because we neglect here all effects from parasitic collisions, the APIARY 7.5 design is essentially identical to the APIARY 6.3D design.

The transparency conditions (2.24) imply a pairwise equality of the nominal beam-beam parameters, namely $\xi_{0x+} = \xi_{0x-}$ and $\xi_{0y+} = \xi_{0y-}$ with ξ_{0x} in general different from ξ_{0y}. The parameters in Table 1 do satisfy the transparency conditions; however, their values imply an additional equality on the nominal beam-beam parameters, namely

$$\xi_{0x+} = \xi_{0x-} = \xi_{0y+} = \xi_{0y-} = 0.03 \tag{2.32}$$

The limiting forms (2.17) and (2.19) for the solution are

$$Y_+ \ [\mu\text{m}] = \begin{cases} 0.0211d \ [\mu\text{m}] + \mathcal{O}(d^2) & \text{for small } d \\ 60.4/d \ [\mu\text{m}] + \mathcal{O}(d^{-2}) & \text{for large } d \end{cases} \tag{2.33}$$

and the orbit deflections are, in these limits,

$$\Delta Y'_+ \ [\mu\text{rad}] = \begin{cases} -12.6d \ [\mu\text{m}] + \mathcal{O}(d^2) & \text{for small } d \\ -0.0360/d \ [\mu\text{m}] + \mathcal{O}(d^{-2}) & \text{for large } d \end{cases} \tag{2.34}$$

while the corresponding quantities for the electron beam are obtained from Eq. (2.25) as

$$Y_- = -Y_+ , \qquad \Delta Y'_- = -\tfrac{1}{2}\Delta Y'_+ \tag{2.35}$$

Because of the smallness of ξ_0 and because of the proximity of ν_y to the half-integer, the orbit offset has small sensitivity to d, as evidenced by the smallness of the coefficient 0.0211 in Eq. (2.33). Fig. 3a shows the result of solving numerically the closed-orbit equations (2.10) for a range of values of d; it can be seen that the largest value of the offset is ~ 0.26 μm which occurs for $d \simeq 25\mu$m. Fig. 3b shows an expanded view of the LER offset Y_+ plotted *vs.* d and *vs.* the true orbit separation, $d + Y_+ - Y_-$. This figure also shows the small-d approximation, Eq. (2.17). Fig. 3c shows the LER offset for larger values of d, and the large-d approximation, Eq. (2.19). Fig. 4 shows the true orbit separation $d + Y_+ - Y_-$ plotted *vs.* d. The fact that it is almost a straight line along the diagonal is, again, a reflection of the smallness of Y_+ and Y_-. Fig. 5 shows the orbit deflections $\Delta Y'_\pm$ plotted *vs.* d, showing the –2:1 relation, Eq. (2.35).

Let us now consider the weak-strong case, for which the numerical solution is shown in Figs. 6 and 7. As explained in Sec. 2.4, we have taken as the "weak beam" a single positron. Fig. 6 shows the positron orbit offset, and Fig. 7 shows the positron orbit deflection at the IP, $\Delta Y'_+$, along with the results of a single-particle tracking calculation with Tennyson's code.[15] In this calculation we assume

the nominal HER beam parameters listed in Table 1. The positron is tracked for a few hundred turns; its phase space coordinates, accumulated turn by turn, define an elliptical curve, the center of which is used to calculate the deflection angle. The result is displayed in Fig. 7 (crosses) superimposed on the numerical solution of Eqs. (2.20)-(2.9) (solid line).

2.9. Rule of thumb for the maximum orbit distortion

From the analytical and numerical solutions presented above, one sees that the largest orbit distortion and the largest beam deflection, in absolute value, can be estimated by

$$\begin{aligned} (Y_{\pm})_{\max} &\simeq 2\pi\Xi_{y\pm}\Sigma_y \cot(\pi\nu_{y\pm}) \\ (\Delta Y'_{\pm})_{\max} &\simeq 4\pi\Xi_{y\pm}\frac{\Sigma_y}{\beta^*_{y\pm}} \end{aligned} \tag{2.36}$$

For the APIARY 7.5 case these expressions underestimate the true maxima by $\sim 15-30\%$. For rounder beams the underestimate would be larger than this, perhaps as much as $\sim 50\%$. In any case, these expressions provide a reasonable rule of thumb for the largest effect one should expect.

For the weak-strong case the above expressions are still valid provided one makes the appropriate substitutions $\Sigma \to \sigma$ and $\Xi \to \xi$.

3. The map in the frequency domain

In order to assess dynamical features of the coherent dipole mode of the beam-beam interaction we iterate the map (2.5)-(2.6) from an initial condition that is slightly away from the fixed point found from the closed-orbit equations (2.10). Physically, this corresponds to kicking the beams away from their equilibrium orbits and observing the subsequent motion turn by turn. We store the coordinate Y_- of the centroid of the electron beam for 512 turns and use this set of values to perform a fast Fourier transform (FFT). In this calculation, as in the previous ones, the beam sizes are assumed to remain unaffected at their nominal values (Table 1).

Figure 8 shows the spectrum for a large vertical bump of $d = 50\ \mu$m. Due to the properties of the FFT, the spectrum peaks at the mirror frequency $1-0.57 = 0.43$ rather than 0.57. The fact that d is fairly large compared to Σ_y implies that the beams are approximately decoupled, hence the appearence of the fundamental frequency only.

Figure 9 shows the same spectrum for head-on collisions, $d = 0$. In addition to the σ mode at 0.43, a second line, the π-mode, is clearly visible. If $\nu_{y+} = \nu_{y-}$ it can be shown that, to lowest order in Ξ and for small-amplitude oscillations about the closed orbit, the $\sigma - \pi$ tune split $\Delta\nu \equiv \nu_\sigma - \nu_\pi$ is given by[8]

$$\cos(2\pi(\nu_y + \Delta\nu)) = \cos(2\pi\nu_y) - 2\pi(\Xi_{y+} + \Xi_{y-})\sin(2\pi\nu_y) \qquad (3.1)$$

For $\nu_y = 0.57$ and $\Xi_{y+} = \Xi_{y-} = 0.015$ this equation yields $\Delta\nu = 0.026$, which is in agreement with the observed difference between the tunes of the two peaks in the FFT.

The location of the two peaks as a function of the bump amplitude d is shown in Fig. 10. Clearly, for large beam separation there is no coupling between the two beams. Reducing the bump amplitude to smaller values increases the $\sigma - \pi$ tune split.

Repeating the same analysis for a *horizontal* bump scan gives a surprising result, shown in Fig. 11. For almost head-on collisions the graph exhibits the same features as Fig. 10. As the bump amplitude is increased, however, the splitting between π and σ modes vanishes and then the π-mode appears on the other side of the tune. We interpret this by observing that the coupling between the two oscillating beams is proportional to the slope of the mutual deflection curve. The crossing of the modes at $d_x \simeq 350\,\mu$m corresponds to the peak of the horizontal beam-beam deflection curve, shown in Fig. 12. At an extremum the deflection acts just as a dipole kick for both beams, but small oscillations around it "see" the same deflection angle; therefore the tunes are not coupled. Furthermore, the slopes of the deflection curve on either side of the extremum have opposite sign and therefore the tune split changes sign. This effect is not visible for vertical scans because the slope of the deflection curve does not turn rapidly enough after the extrema are reached. The reason for this is, of course, the large aspect ratio of the beams.

We emphasize that we have only analyzed the dipole mode of the beams, *i.e.*, the coherent behavior of rigid beams. In reality, or in more complete calculations,[16,17] the $\sigma - \pi$ tune split is different from the result stated here because of higher-order mode effects.

4. Multiparticle tracking calculations

So far we have presented results under the assumption that the beam sizes are fixed and equal to their nominal values. In reality, however, the beam sizes depend on the bump amplitude d. Furthermore, we have neglected synchrotron motion and all longitudinal effects in the beam-beam collision (thick-lens effects). In this section we present "strong-strong" multiparticle tracking simulations that correct these deficiencies. We have carried out simulations with Yokoya's code[18] and with Tennyson's code.[15] These two codes use different kinds of approximations that are needed in simulations with a finite number of particles. The results shown below are in qualitative agreement, and the quantitative differences give us an idea of the accuracy that can be expected of these kinds of simulations.

In the simulations with Yokoya's code, the bunches are represented by 200 "superparticles" each. Thick-lens effects are taken into account by dividing the bunches up in the longitudinal direction into 5 slices located at $z = 0$, $\pm\sigma_\ell$ and $\pm 2\sigma_\ell$. This "slicing" of the bunch takes care of the phase averaging during the collision.[19] Previous experience in PEP-II simulations[1] suggests that five slices is a reasonable number to use with this code. This represents a compromise between a desire for accuracy, requiring many slices, with the constraints of computational expense, requiring few slices. When fewer than five slices are used, the results tend to show an artificially large beam blowup. The superparticles undergo synchrotron oscillations at a specified tune ν_s. The simulations were carried out for 25,000 turns, or about 5 damping times. The beam sizes and beam centroid positions and deflection angles were determined by averaging over the last 10,000 turns of the run, sampling at every turn. The exact values of the parameters used in these simulations differ slightly from those in Table 1, and are listed at the right margin of the corresponding figures.

At the beginning of the run the superparticles are Gaussian-distributed in phase space. At every turn thereafter the distribution necessarily deviates from Gaussian, at least to some extent, due to the nonlinear force. Nevertheless, for the purposes of calculating the beam-beam force, we assume the distribution to be Gaussian. The algorithm is the following: at every turn we compute the centroid and σ's of the particle distribution, and then use Eq. (2.3) to obtain the beam-beam kick on each superparticle of the opposing bunch.

Figure 13 shows the rms beam sizes, normalized to their nominal values, obtained from the simulation.

Figure 14 shows the beam centroid offset Y. Three sets of data are plotted. The solid lines are the true offsets, obtained by measuring the beam centroid position from the simulation. The dashed lines are the offsets calculated from the

closed-orbit equations (2.10), but using the actual blown-up beam sizes obtained from the simulation (shown in Fig. 13). The dotted lines are the offsets calculated from Eqs. (2.10) assuming the nominal beam sizes listed in Table 1 (*i.e.*, no beam blowup).

Figure 15 shows the beam centroid deflections $\Delta Y'$. The three sets of curves shown correspond to the same conditions as in the preceding paragraph.

In Figs. 14 and 15 the solid and dashed curves are not expected to be identical because thick lens effects are fully taken into account only in the simulation case (solid curves). The fact that these curves are so close to each other means that, in our particular case, thick lens effects are important only inasmuch as they influence beam size. It is known that thick lens effects are important[19] in higher-order modes. Another set of simulations (not presented here) shows that the beam blowup is a factor ~ 2 larger in the thin-lens approximation (one longitudinal slice) than in the thick-lens case with 5 longitudinal slices.

In the simulations with Tennyson's code the beams are represented by 256 superparticles each, and thick lens effects are taken into account using 5 slices located at $z = 0$, $\pm\frac{7}{12}\sigma_\ell$ and $\pm\frac{7}{6}\sigma_\ell$. As in the case with Yokoya's code, the simulations were carried out for 25,000 turns, and the beam sizes and centroid positions were obtained by averaging over the last 10,000 turns of the run; the sampling, however, was done every 50 turns. The exact values of the parameters used were slightly different from those previously used, and are listed at the right margin of the corresponding figures.

Figure 16 shows the results for the beam blowup factors obtained from the simulation. The blowup factor reaches a maximum of ~ 2, which is somewhat larger than the result obtained with Yokoya's code. We attribute the difference between these results to the minor differences in the values of the damping times and other beam parameters assumed in the two calculations, (compare parameters at the right margins of the corresponding figures), and to differences in the mathematical approximations underlying the two codes. In particular, Tennyson's code concentrates the slices closer to the origin than does Yokoya's code, thus resembling more the thin-lens case which, as mentioned earlier, entails more beam blowup.

Figures 17 and 18, respectively, display the beam centroid offsets and their deflections as extracted from the full simulation and from the analytical calculation, either with blown up or with nominal beam sizes. The statistical fluctuations are larger than in Yokoya's code because the beam size average is computed by sampling every 50 turns rather than every turn. This is reflected in the lack of smoothness of the curves in these figures, compared to the results displayed in Figs. 14 and 15.

In summary, both simulations suggest that the vertical positron spot size blows up by a factor of 1.5 to 2 when the beams are separated by about one to three times the vertical RMS beam size. The vertical electron spot size increases by only 15% to 25% in the same range of separations, and the horizontal beam sizes remain essentially unaffected by vertical beam separation at the IP. The closed orbit distortion, in turn, is well described by the analytical one-turn map approach, provided one takes into account the effective beam blowup predicted by the simulations. Finally, the magnitude of the beam centroid offsets and deflections, and their dependence on the beam separation, differ by at most 10% when comparing the naive, rigid bunch analytical calculation of Sec. 2 to the full simulation described in the present section.

5. Discussion of experimental feasibility

While the closed orbit distortion at the IP is very small for the nominal PEP-II design (Figs. 14, 17) under normal operating conditions, the beam-beam-induced angular deflection (Figs. 15, 18) represents a sizeable fraction ($\sim$ 30%) of the angular divergence σ'^{*}_{0y} of the beam. The orbit distortion should therefore become measurable at points away from the IP, where favorable phase relationships and large enough beta functions provide the necessary amplification. If sufficient beam position monitors (BPMs) are available at well-chosen locations around the ring, then the dependence of the closed-orbit distortion on the IP beam separation could be exploited[20] to optimize the optical functions at the IP following a procedure similar to that used at the SLC.[6,7]

A proposal has been put forth to test these ideas experimentally at the TRISTAN ring at KEK.[21] We present here the corresponding results of the analytical calculations and multiparticle simulations similar to those in Sec. 4. We also present a brief summary of the error analysis bearing on the feasibility of such an experiment.[20] The assumed parameters for the TRISTAN ring are summarized in Table 2.

The values in Table 2 imply nominal beam-beam parameters $\xi_{0x+} = \xi_{0x-} = 0.018$ and $\xi_{0y+} = \xi_{0y-} = 0.025$, that are smaller than those for PEP-II ($\xi_0 = 0.03$). However, since the vertical tune is closer to the integer, the closed orbit distortion due to the beam-beam interaction is larger for TRISTAN.

Figure 19 shows the true orbit separation $d + Y_+ - Y_-$ plotted *vs.* d computed analytically in the rigid-Gaussian bunch approximation. Results from multiparticle tracking simulations with Yokoya's code are shown in Figs. 20–22 (these are the analogues of Figs. 13–15 for PEP-II). The beam blowup in the case of TRISTAN

Table 2. Parameters for TRISTAN simulations (Yokoya's code).

	e^+ and e^-
E [GeV]	29.0
N	1.885×10^{11}
β_x^* [cm]	100
β_y^* [cm]	4.0
σ_{0x}^* [μm]	284.6
σ_{0y}^* [μm]	8.050
$\sigma_{0x}'^*$ [mrad]	0.285
$\sigma_{0y}'^*$ [mrad]	0.201
σ_ℓ [cm]	1.5
σ_E/E	2.33×10^{-3}
ν_s	0.113
τ_x [turns]	110
τ_y [turns]	228
τ_ℓ [turns]	228
ν_x	0.61
ν_y	0.72

(Fig. 20) is quite modest ($\lesssim 10\%$) so the difference between the analytical results and multiparticle simulations is very small.

In order to carry out an error analysis, we make the following simplifying assumptions: (a) equal BPM errors for all BPMs, (b) equal beta functions $\hat{\beta}$ at the BPMs and (c) random average betatron phases at the BPMs. It can then be shown that the error with which one can determine the deflection angle is given by[20]

$$\sigma(\Delta Y') \simeq \frac{2\sqrt{2}\,\sin(\pi\nu_y)}{\sqrt{\beta_y^*\hat{\beta}}}\,\frac{\sigma_{\rm BPM}}{\sqrt{N}} \qquad (5.1)$$

where N is here the total number of BPMs and $\sigma_{\rm BPM}$ is the rms measurement error of the BPMs. Using the parameters from Table 2 and $\hat{\beta} = 20$ m and $N = 100$, which are typical values for TRISTAN, we obtain

$$\sigma(\Delta Y')\ [\mu\text{rad}] \simeq 0.25\,\sigma_{\rm BPM}\ [\mu\text{m}] \qquad (5.2)$$

Consequently, a 5 μm BPM error leads to $1-2\,\mu$rad error in the vertical deflection angle. A similar analysis shows that the error bars for the horizontal deflection

curve are $\lesssim 0.5\,\mu$rad. The amplification factor for the closed orbit distortion, $Y(\mathrm{BPM})/Y(\mathrm{IP})$, is $\simeq 25$; therefore the error by which the orbit separation at the IP can be determined is small ($\sim 0.2\,\mu$m) compared to its maximum value ($\sim 1\,\mu$m). This error is probably dominated by the jitter of the power supply for the separator plates.

We have computed the deflection curves from Eqs. (2.8), (2.9) and (2.10) and fitted an approximate expression, valid for $\Sigma_x/\Sigma_y \gg 1$, given by

$$\Delta Y' \simeq -\frac{2Nr_0}{\gamma\Sigma_x}\left\{\sqrt{\frac{\pi}{2}}\,\mathrm{erf}\left(\frac{y-y_0}{\sqrt{2}\Sigma_y}\right) - \frac{y-y_0}{\Sigma_x}\right\} \tag{5.3}$$

where y is the perturbation applied to beam by the closed bump and y_0 is the initial separation between the beams before the scan. Given the above estimates for the accuracy of the measurements, the spot size Σ_y and the position of the beam centroid y_0 can be measured with an accuracy of about 1 micron. This precision makes the beam-beam deflection method quite promising in its applications to IP spot size determination, as well as to feedback systems that maintain the beams in collision.

6. Conclusions

We have presented an analysis of the beam-beam effect on the closed orbits for asymmetric colliders, and studied its possible applicability to the determination of the spot size and the beam separation at the IP. An error analysis suggests that this method is a promising diagnostic and feedback tool for beam collisions. This technique is intended to complement other methods in the optimization of the luminosity performance of the collider.

In this analysis we have neglected all effects from the parasitic collisions. We believe that these effects will not change our results qualitatively. In a future note we intend to present more detailed multiparticle tracking simulations that will include parasitic collisions.

A proposed experiment at TRISTAN will allow us to assess the feasibility of this method and to calibrate our calculations in a more realistic fashion.

Acknowledgements: We thank H. DeStaebler, A. Hutton and R. Siemann for helpful discussions, and M. Zisman for a careful reading of the compuscript.

REFERENCES

1. "An Asymmetric B Factory Based on PEP–Conceptual Design Report," LBL PUB-5303/SLAC-372/CALT-68-1715/UCRL-ID-106426/UC-IIRPA-91-01, February 1991.
2. Minutes of the B factory IP Instrumentation Jamboree held at SLAC, August 22, 1991 (unpublished).
3. C. Field and W. Kozanecki, "Wire Scanners at the B Factory," ABC-55.
4. H. DeStaebler, "A Fast Relative Luminosity Monitor," ABC-56.
5. P. Bambade, R. Erickson, W. A. Koska, W. Kozanecki, N. Phinney, and S.R. Wagner, "Observation of Beam-Beam Deflections at the Interaction Point of the SLAC Linear Collider," SLAC-PUB-4767-Rev., April 1989.
6. F. Rouse, T. Gromme, W. Kozanecki, N. Phinney, "Maintaining Micron-Size Beams in Collision at the Interaction Point of the Stanford Linear Collider," SLAC-PUB-5512, presented at the IEEE Particle Accelerator Conf., San Francisco, CA, May 6-9, 1991, p. 3222.
7. W. A. Koska, P. Bambade, W. Kozanecki, N. Phinney, S.R. Wagner, "Beam-Beam Deflection as a Beam Tuning Tool at the Slac Linear Collider," Nucl. Instr. Meth. **A286**, 32 (1990); N. Phinney, P. Bambade, W. Kozanecki and W. A. Koska, "An Automated Focal Point Positioning and Emittance Measurement Procedure for the Interaction Point of the SLC," Nucl. Instr. Meth. **A288**, 308 (1990).
8. K. Hirata and E. Keil, "Barycentre Motion of Beams due to Beam-Beam Interaction in Asymmetric Colliders," CERN/LEP–TH/89-76, December 21, 1989.
9. V. Ziemann, "Beyond Bassetti and Erskine: Beam-Beam Deflections for Non-Gaussian Beams," SLAC-PUB-5582, June 1991, presented at the 7th ICFA Beam Dynamics Workshop, UCLA, May 13–16, 1991.
10. S. Krishnagopal and R. Siemann, "Field Calculation Algorithm for General Beam Distributions," ABC-43/ESG-172/LBL-31094/SLAC/AP-90, July 29, 1991; "Coherent Beam-Beam Interaction in Electron-Positron Colliders," Phys. Rev. Lett. **67**, 2461 (1991).
11. M. Bassetti and G. A. Erskine, "Closed Expression for the Electrical Field of a Two-Dimensional Gaussian Charge," CERN-ISR-TH/80-06.
12. K. Hirata, "Coherent Betatron Oscillation Modes due to Beam-Beam Interactions," Nucl. Inst. and Meth. Phys. Res. **A269**, 7 (1988).

13. M. Sands, "The Physics of Electron Storage Rings: An Introduction," SLAC-121/UC-28 (ACC), November 1970, Eq. 2.90.

14. A. Garren *et al.*, "An Asymmetric B Meson Factory at PEP," Proc. 1989 Part. Acc. Conf., Chicago, p. 1847; Y. H. Chin, "Symmetrization of the Beam-Beam Interaction," in *Beam Dynamics Issues of High Luminosity Asymmetric Collider Rings*, A. M. Sessler, ed., *AIP Conf. Proc.* **214**, 424; also Y. H. Chin, LBL-27665, 1989; S. Krishnagopal and R. Siemann, "Beam-Energy Inequality in the Beam-Beam Interaction," Phys. Rev. D **41**, 1741 (1990); M. A. Furman, "Luminosity Formulas for Asymmetric Colliders with Beam Symmetries," ABC-25/ESG-161, February 1991 (rev. September 1991).

15. J. Tennyson, undocumented code.

16. R. E. Meller and R. H. Siemann, "Coherent Normal Modes of Colliding Beams," IEEE Trans. Nucl. Sci. **NS-28** No. 3, 2431 (1981).

17. K. Yokoya, Y. Funakoshi, E. Kikutani, H. Koiso and J. Urakawa, "Tune Shift of Coherent Beam-Beam Oscillations," KEK Preprint 89-14.

18. K. Yokoya, undocumented code.

19. S. Krishnagopal and R. Siemann, in *Beam Dynamics Issues of High Luminosity Asymmetric Collider Rings*, A. M. Sessler, ed., *AIP Conf. Proc.* **214**, 278 (1990), and Phys. Rev. **D41**, 2312 (1990).

20. V. Ziemann, "The Accuracy of Beam-Beam Deflection Diagnostics for the SLAC/LBL/LLNL B Factory," ABC-59, February 5, 1992.

21. Y. Funakoshi, W. Kozanecki, Y.-H. Chin, M. Furman, N. Toge and V. Ziemann, "Proposal for Experiments at TRISTAN on Beam-Beam Issues for Future B Factories," ABC-61/ESG-169, in preparation.

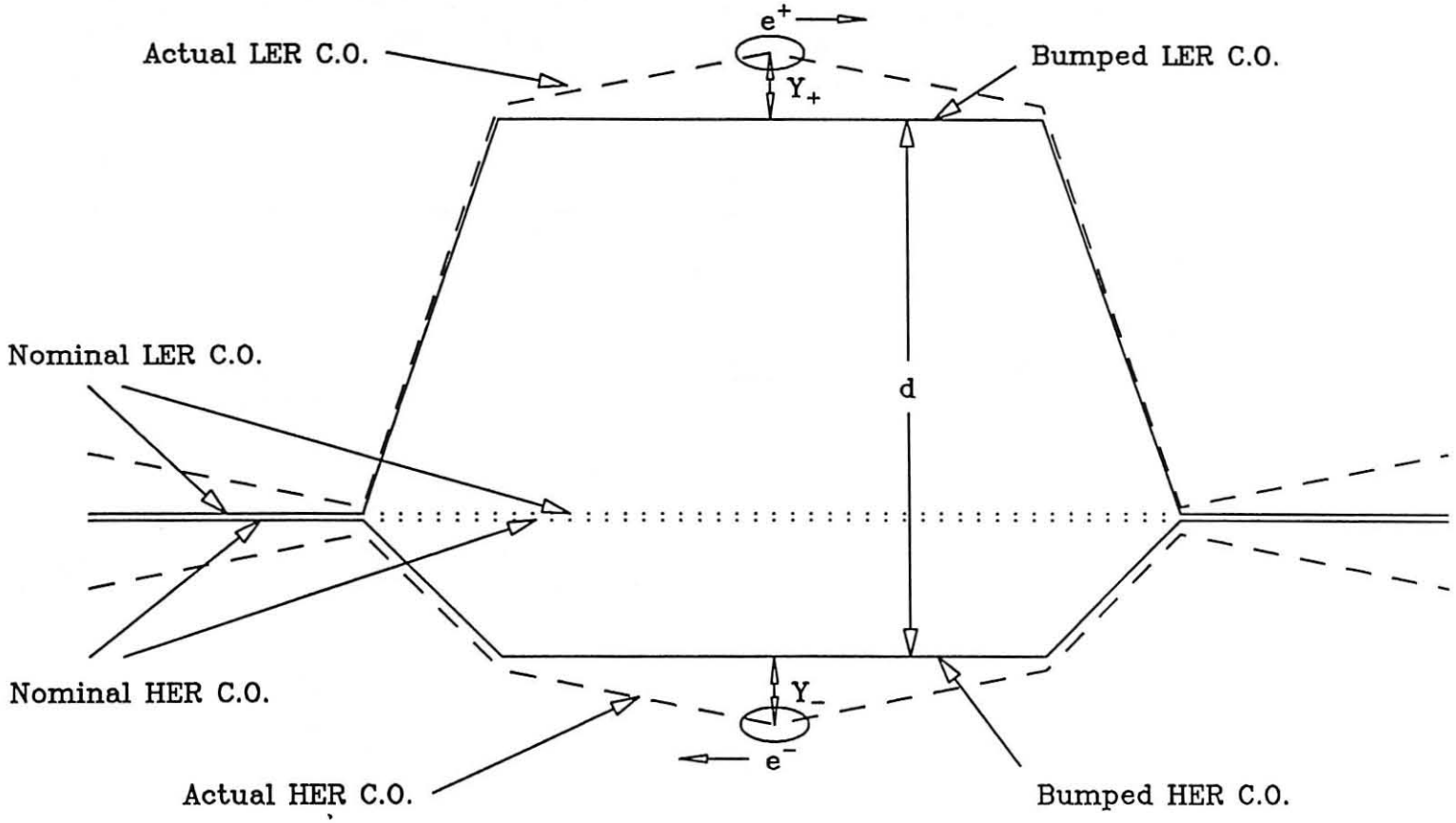

Fig. 1. Elevation sketch of the closed vertical orbit bump in the immediate vicinity of the IP. The nominal closed orbits (C.O.) are indicated by the horizontal solid and dotted lines (shown slightly displaced for the sake of clarity). The two bunches are shown on their actual orbits, displaced by Y_+ and Y_- from their bumped orbits. In this case $Y_+>0$ and $Y_-<0$, so that the actual beam separation is $d+Y_+-Y_-$. The deflections $\Delta Y'_+$ and $\Delta Y'_-$ are <0 and >0, respectively.

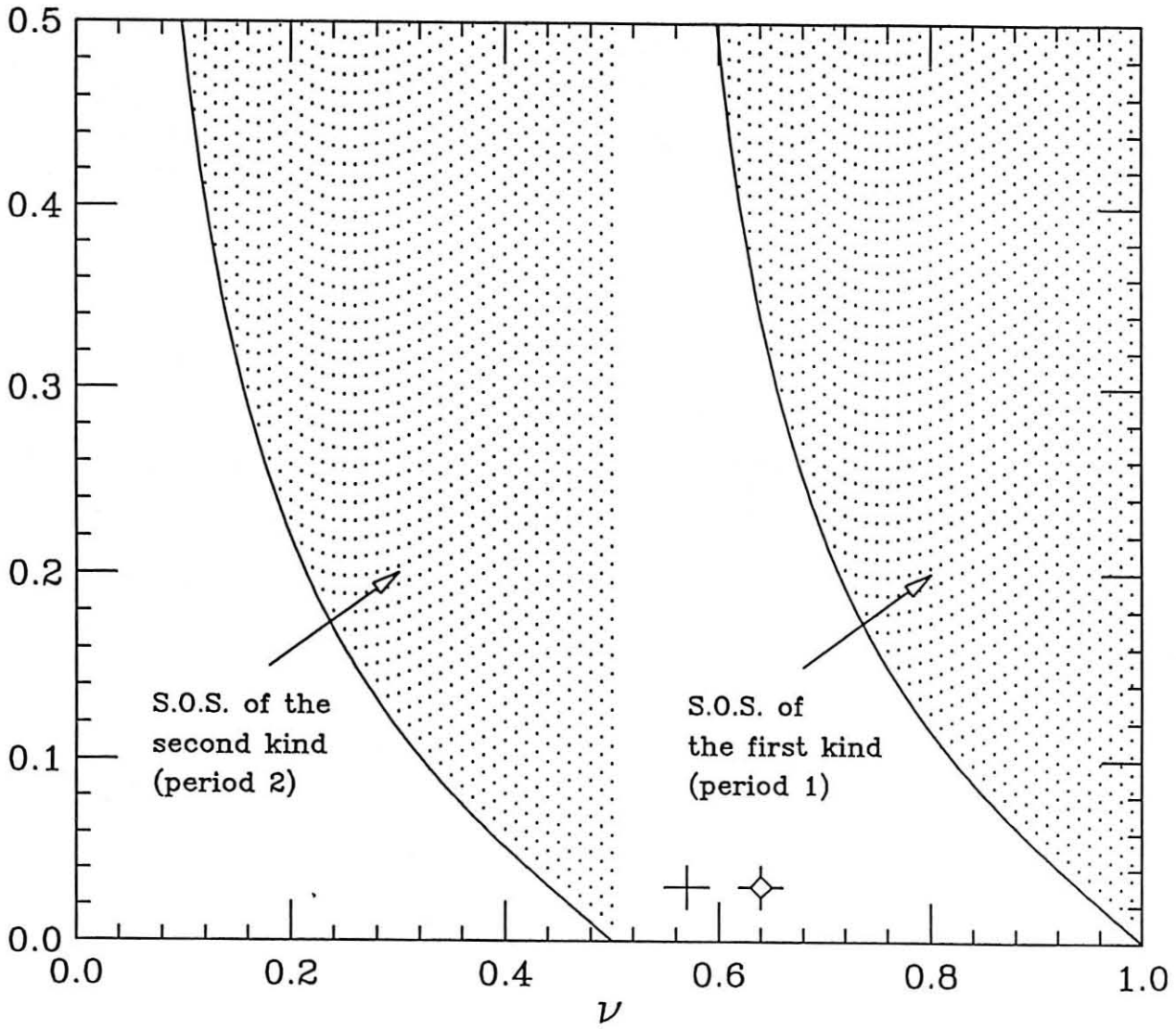

Fig. 2. The shaded domains define the areas of spontaneous orbit separation (S.O.S.), according to Ref. 8. The crosses indicate the operating points for APIARY 7.5 (ν_x=0.64, ν_y=0.57, ξ_x=ξ_y=0.03), both safely away from the undesirable regions.

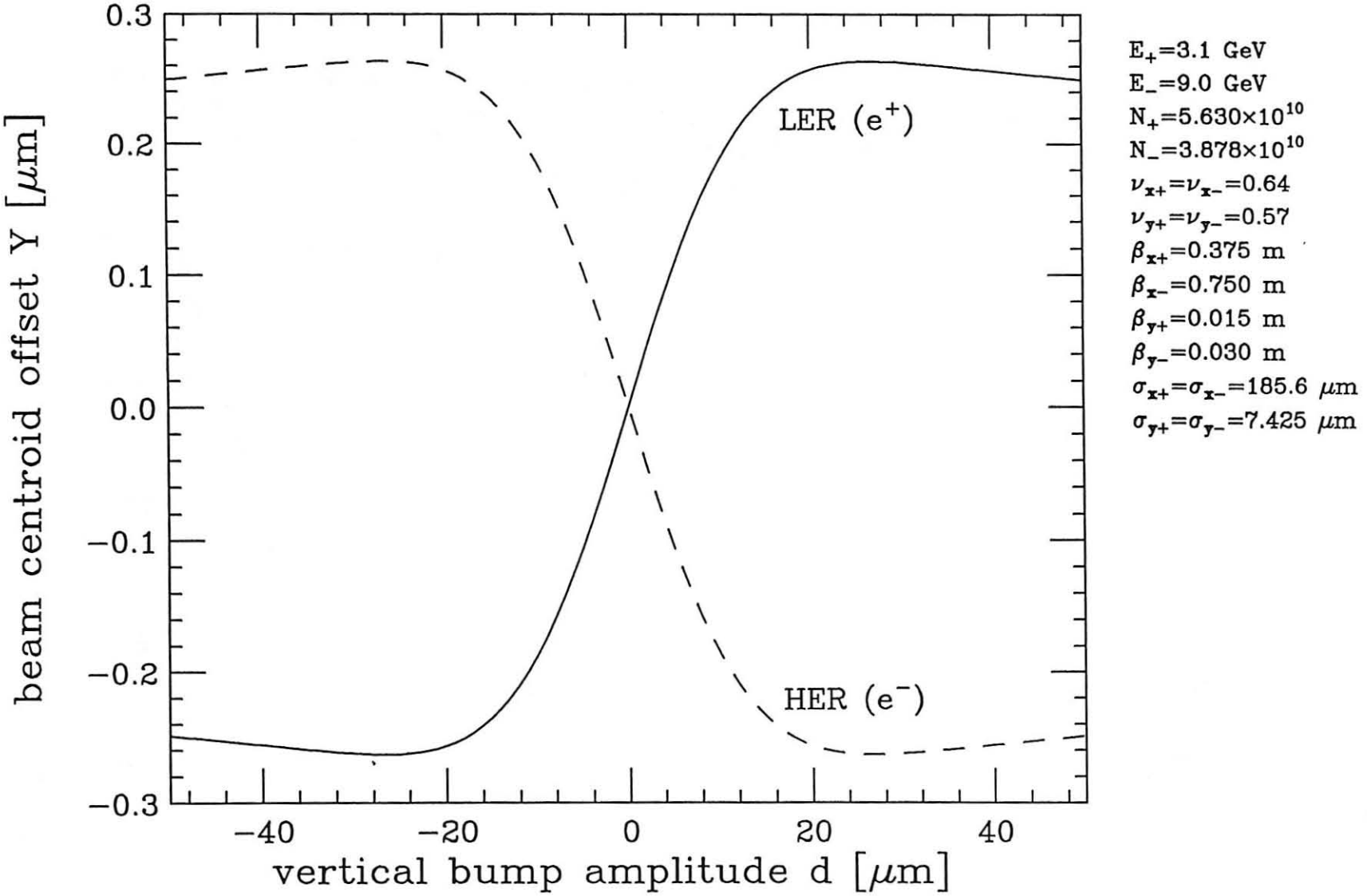

Fig. 3a. Vertical closed orbit distortions for both beams, plotted vs. the nominal vertical bump amplitude d. Note that the distortions are of equal magnitude and opposite sign, as a consequence of transparency symmetry, Eq. (2.35).

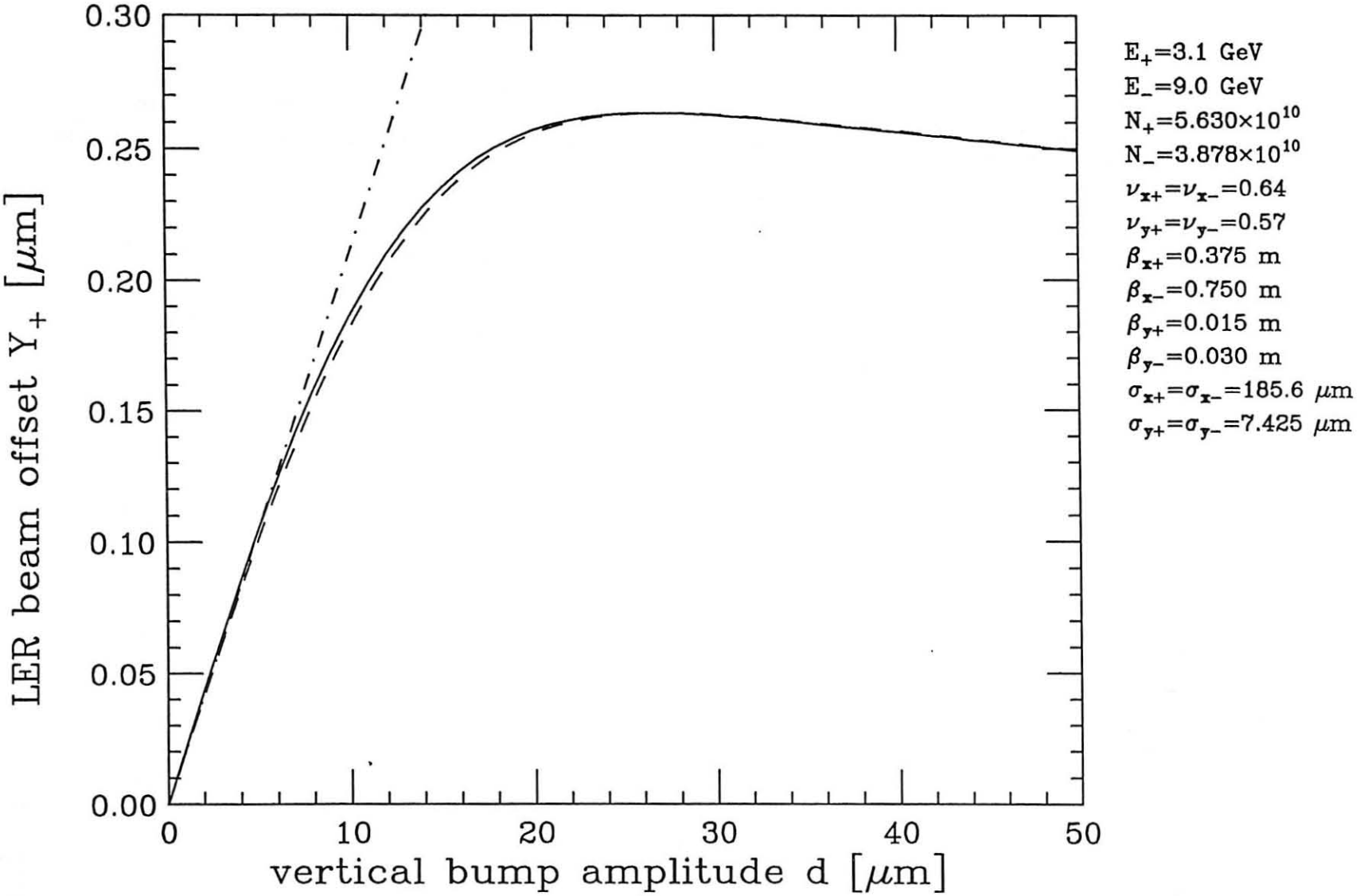

Fig. 3b. Magnified view of the LER orbit offset. The solid line is the same as in Fig. 3a. The dot–dash line is the lowest–order approximation, Eq. (2.17). The dashed line shows the orbit offset plotted vs. the true separation between the orbits, $d+Y_+-Y_-$, rather than d.

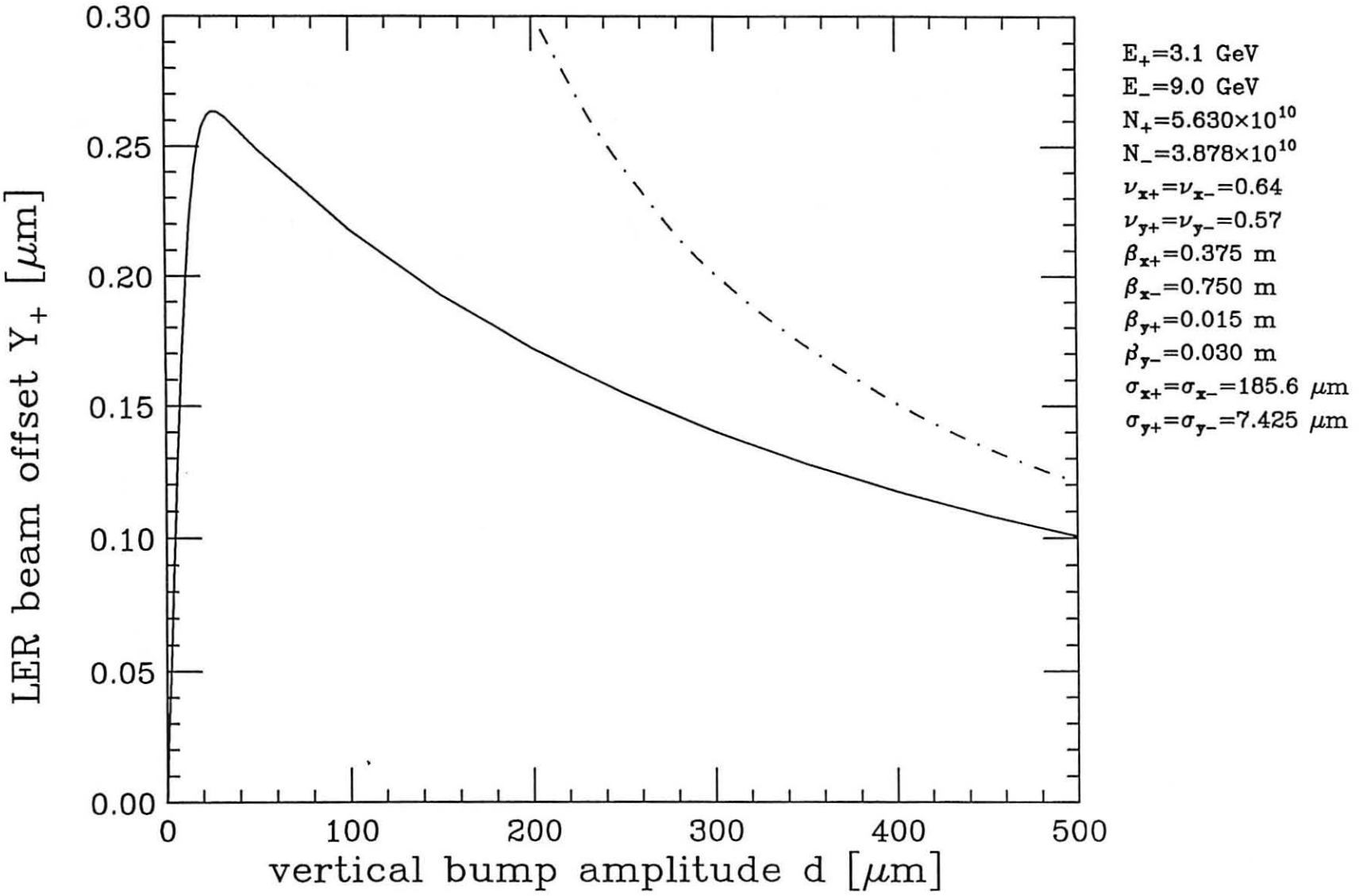

Fig. 3c. LER orbit offset for large values of the bump amplitude. The solid line is the same as in Fig. 3a. The dot–dash line is the asymptotic expression at large d, Eq. (2.19).

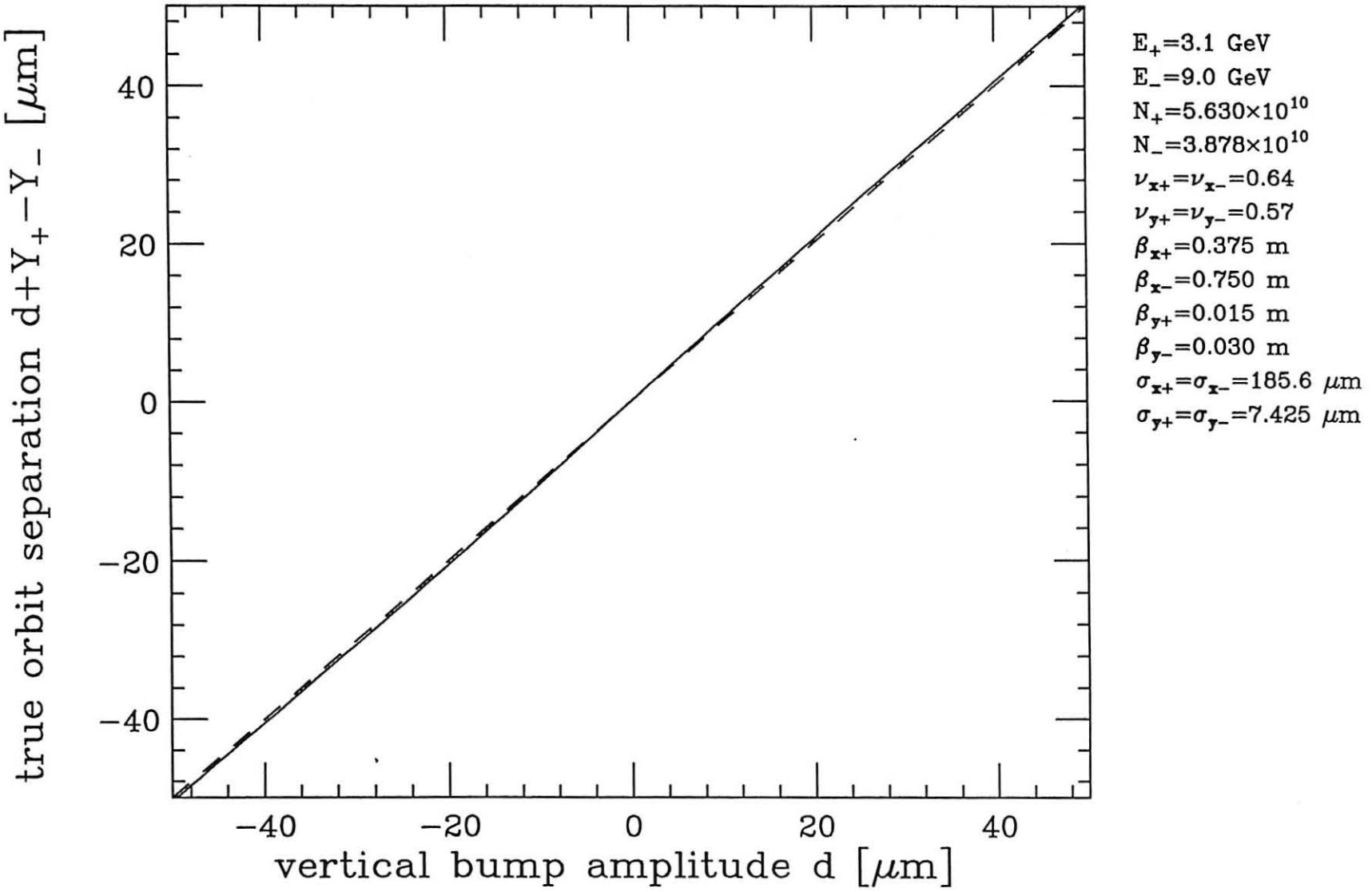

Fig. 4. True orbit separation at the IP (solid line). The dashed line is a straight line along the diagonal, for reference. The fact that the true separation is so close to a straight line is a reflection of the smallnes of the orbit distortions. This smallness is, in turn, a consequence of the smallness of ξ_0 and the closeness of ν_y to the half−integer.

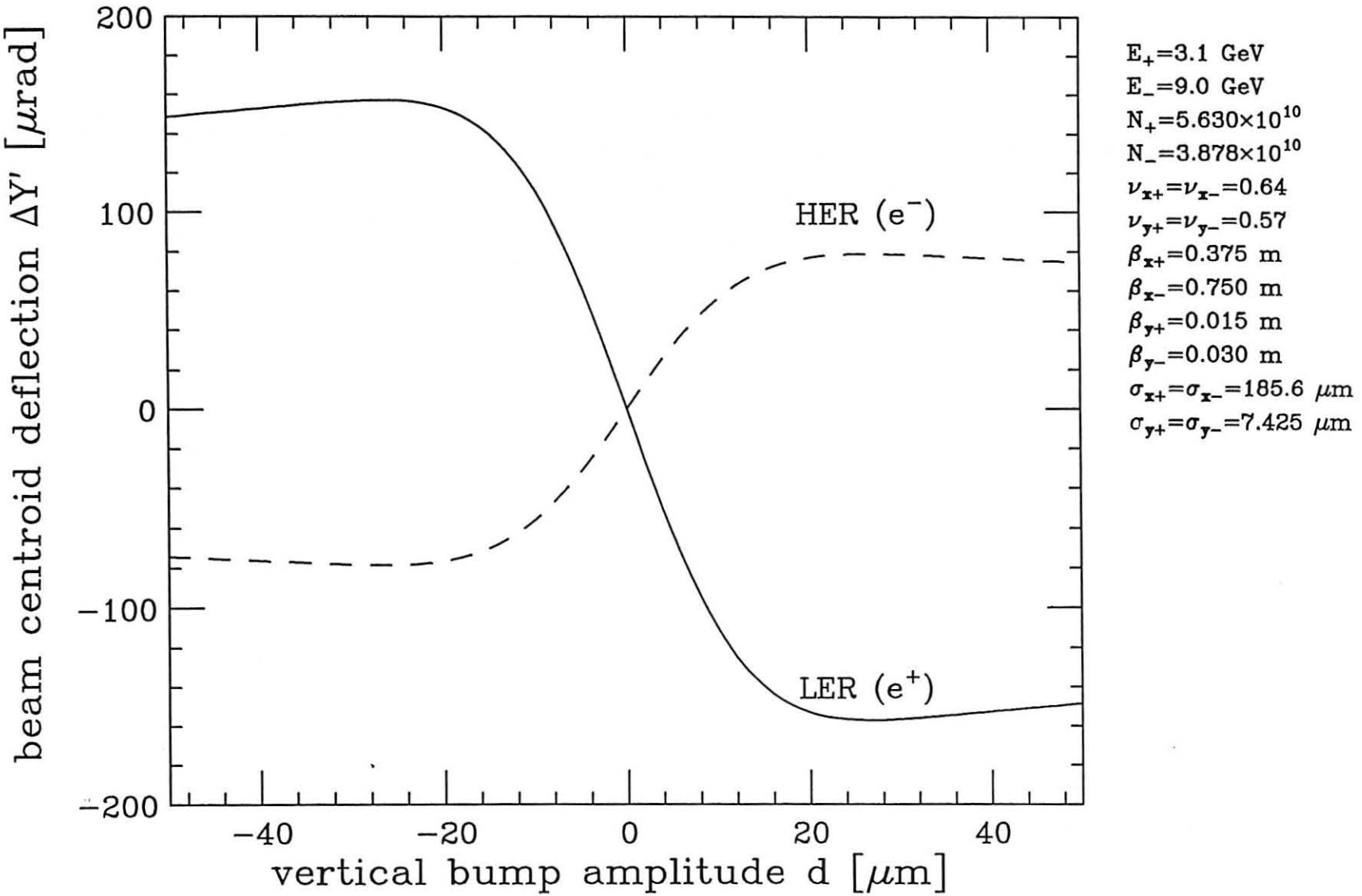

Fig. 5. Angular deflection of the beam centroids at the IP as a result of the beam–beam kick. Note that the deflections are of opposite sign, and the magnitudes are in the ratio 2:1, as a consequence of transparency symmetry, Eq. (2.35).

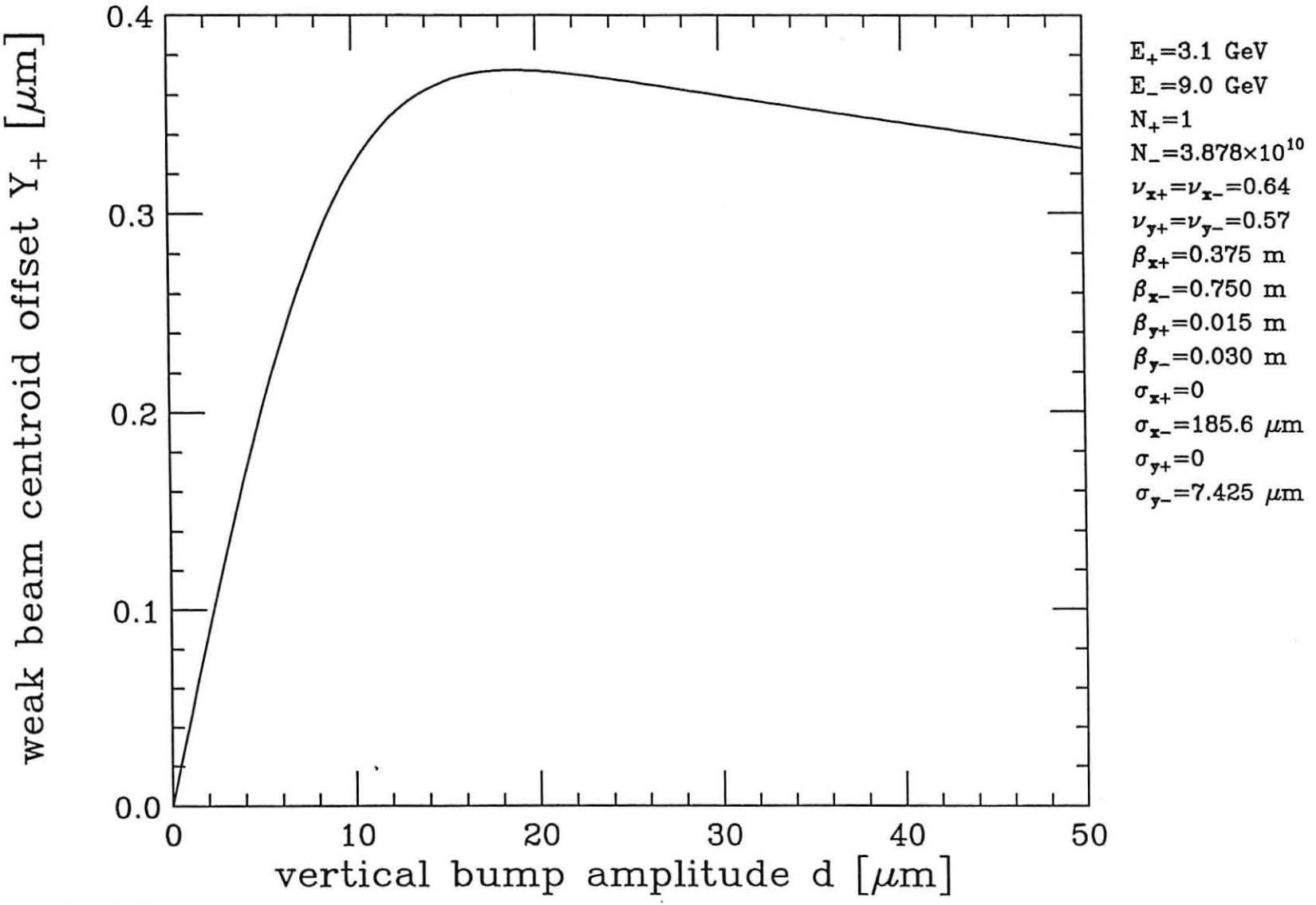

Fig. 6. Vertical closed orbit distortion at the IP of a weak beam consisting of a single positron. In this case the strong beam remains undisturbed.

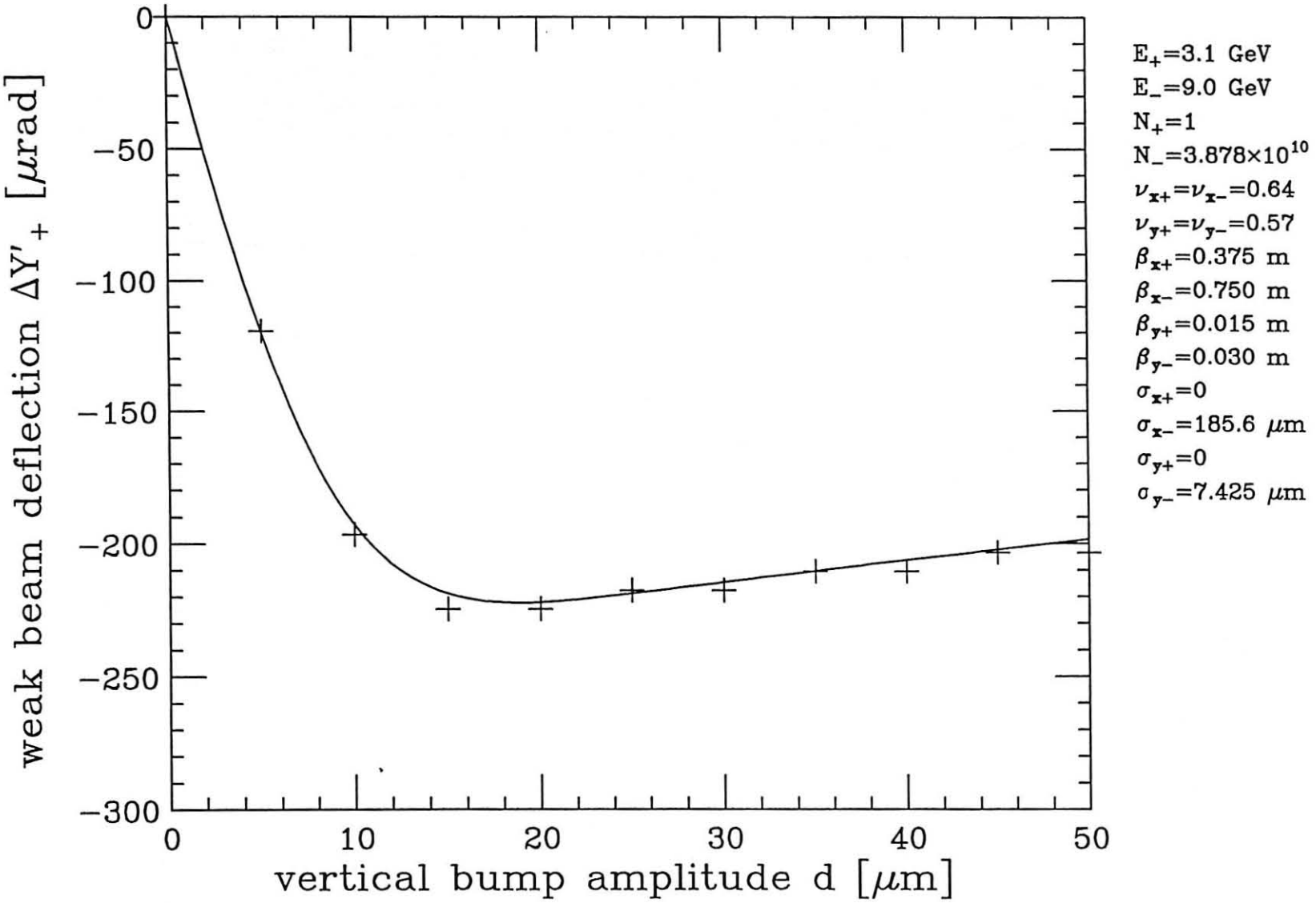

Fig. 7. Angular deflection at the IP of a weak beam consisting of a single positron. The "data points" were obtained by tracking a positron for a few hundred turns with Tennyson's code and then measuring Y' from the resultant phase space plot.

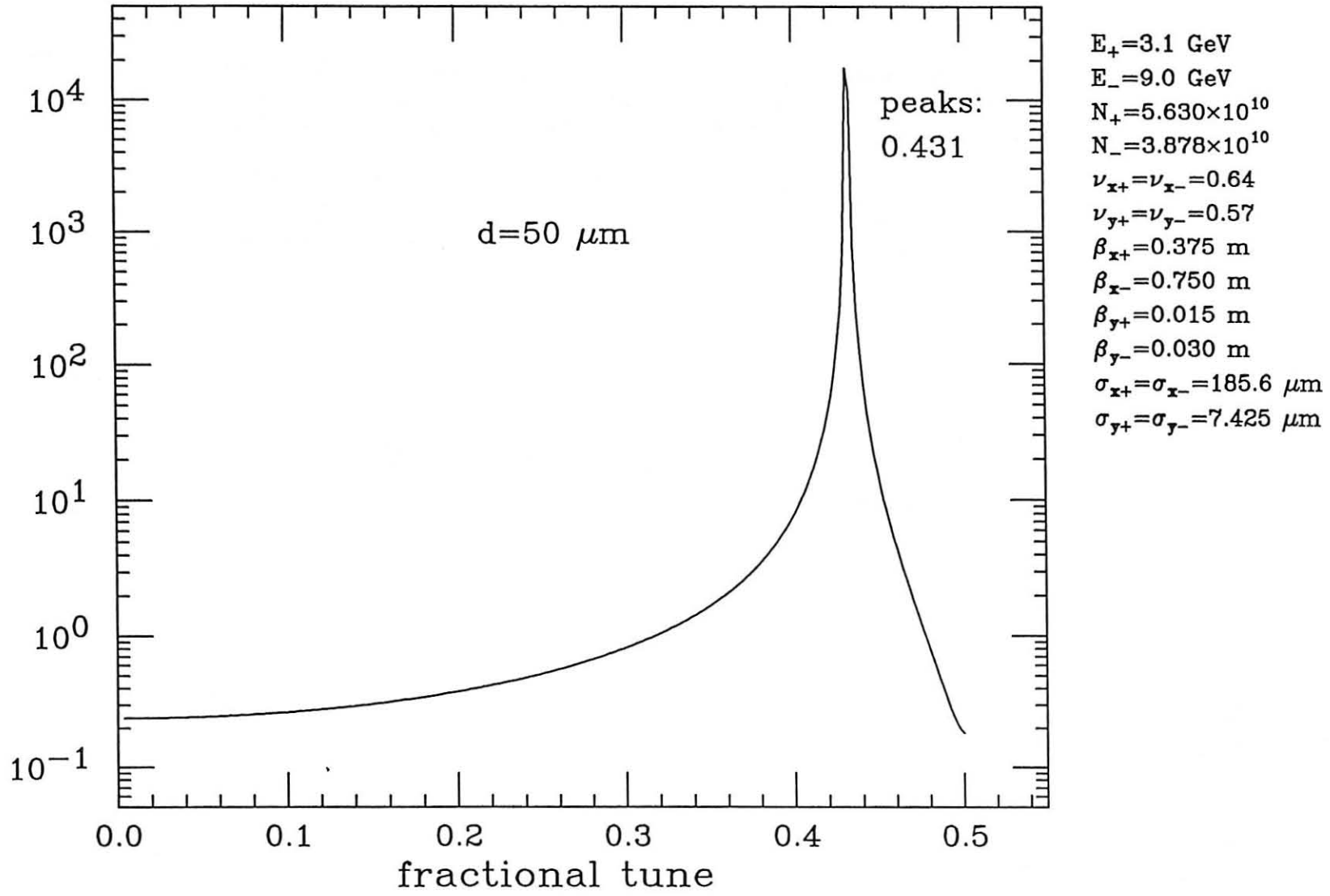

Fig. 8. Frequency spectrum of the vertical motion of the electron bunch centroid, for small–amplitude oscillations about the equilibrium closed orbit. The vertical bump amplitude is d=50 μm. For this relatively large value there is only one peak near the mirror value of the vertical tune, 1−0.57=0.43.

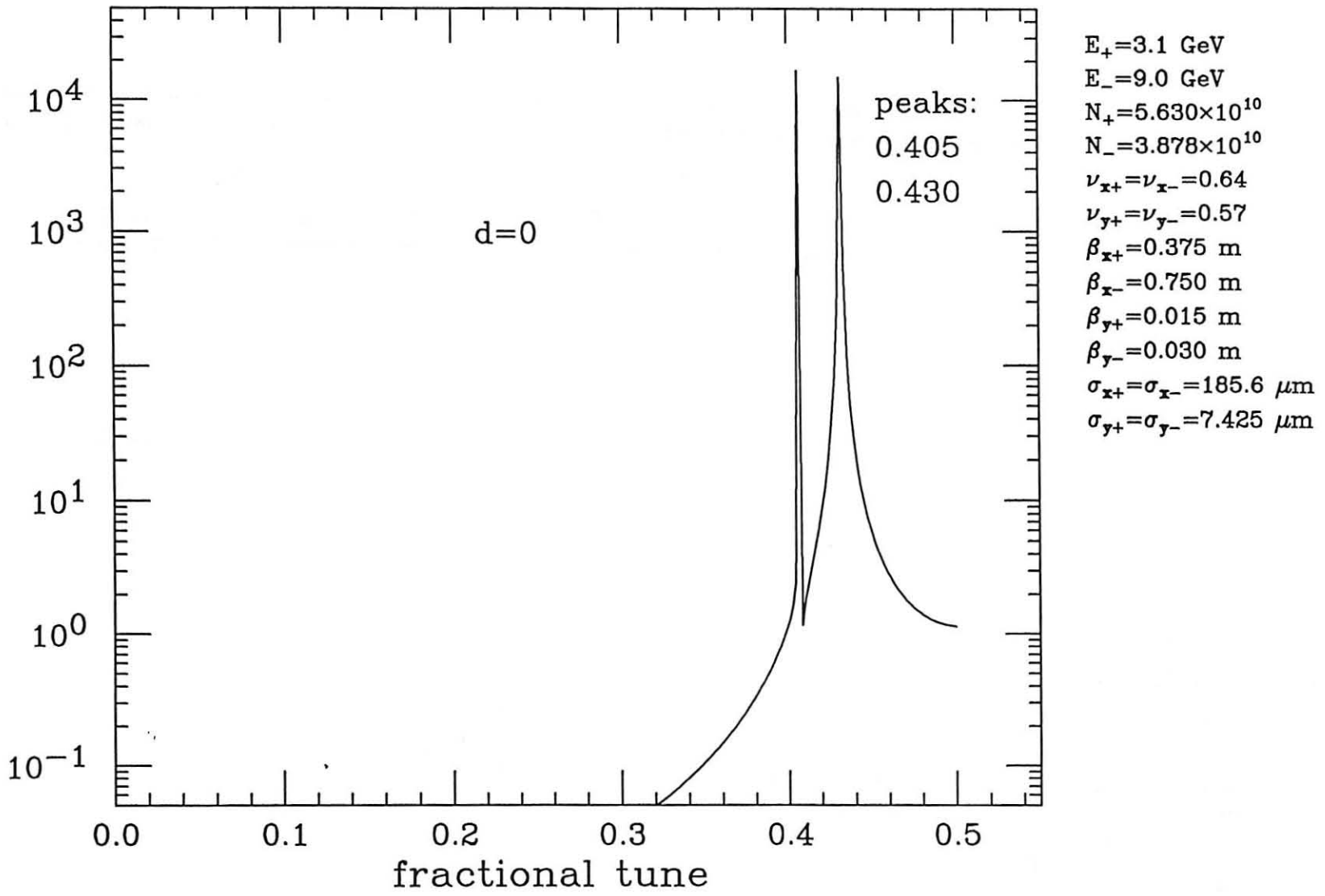

Fig. 9. Frequency spectrum of the vertical motion of the electron bunch centroid for small–amplitude oscillations about the equilibrium closed orbit, for head–on collisions. The peaks at 0.430 and 0.405 correspond to the σ and π modes, respectively. The tune split of 0.025 agrees very well with the analytical result obtained from Eq. (3.1).

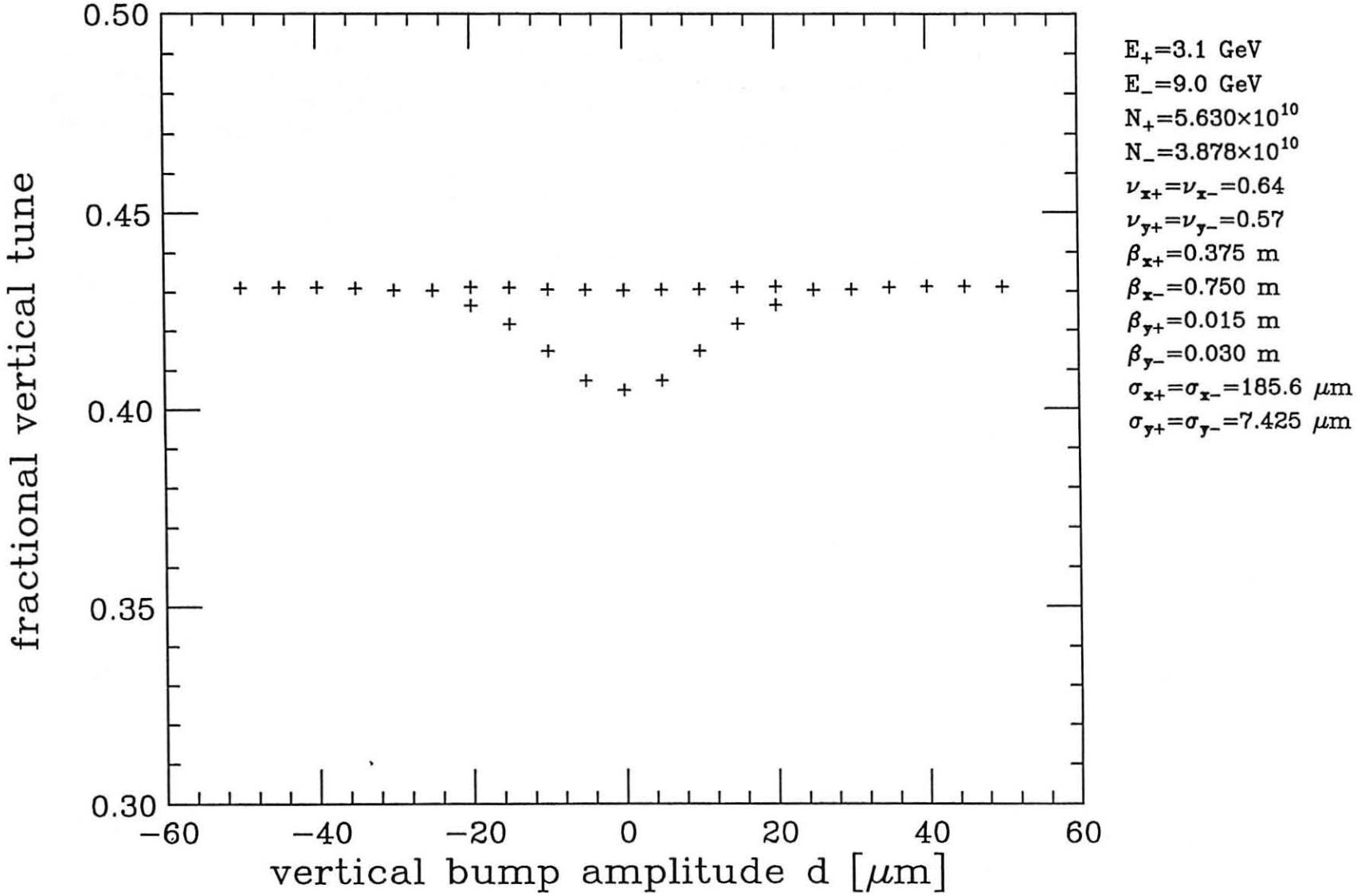

Fig. 10. Position of the σ and π peaks in the frequency spectrum of the vertical motion of the electron bunch centroid, as a function of vertical bump amplitude.

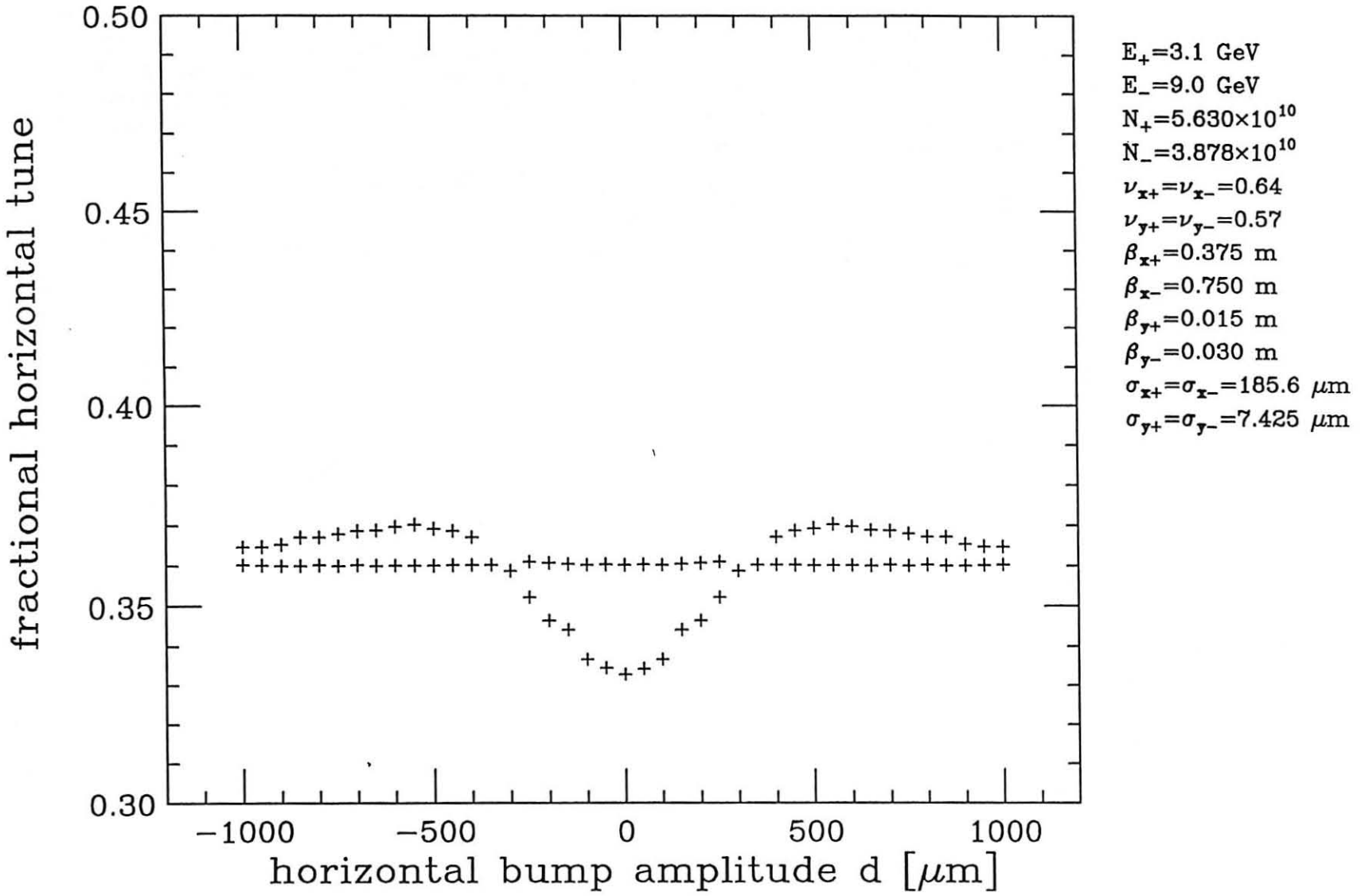

Fig. 11. Position of the σ and π peaks in the frequency spectrum of the horizontal motion of the electron bunch centroid, as a function of horizontal bump amplitude. In this case the vertical amplitude has been set to 0.

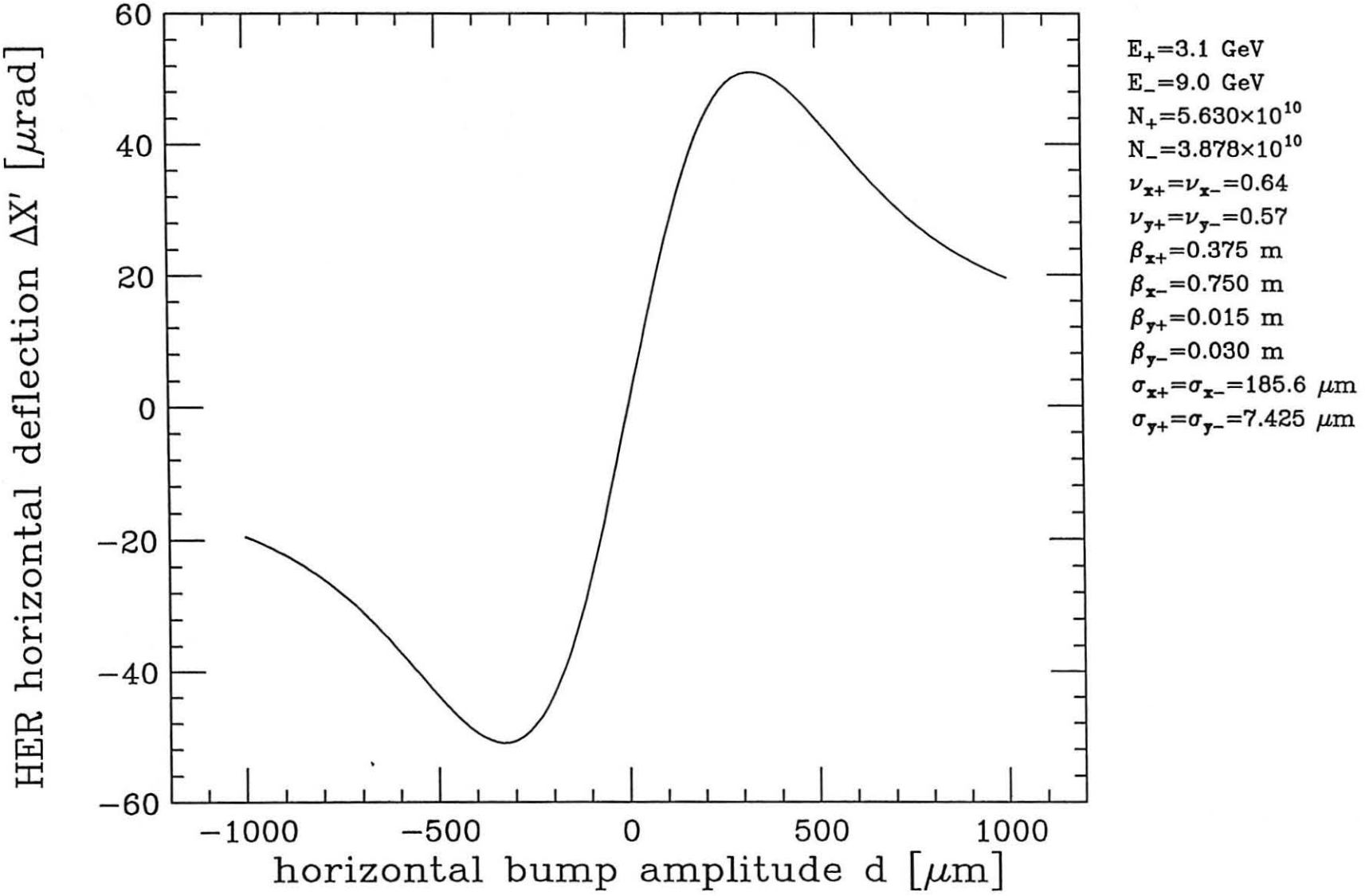

Fig. 12. Angular deflection at the IP of the electron beam centroid as a result of the beam–beam kick for horizontal, rather than vertical, bump amplitudes. Note that the curve falls off more quickly than in the vertical case, Fig. 5. The reason is that, for flat beams ($\sigma_y << \sigma_x$), the scale for the falloff of the beam–beam force in any direction is set by σ_x, while the scale for the rise is set by σ_y in the vertical direction, and by σ_x in the horizontal direction.

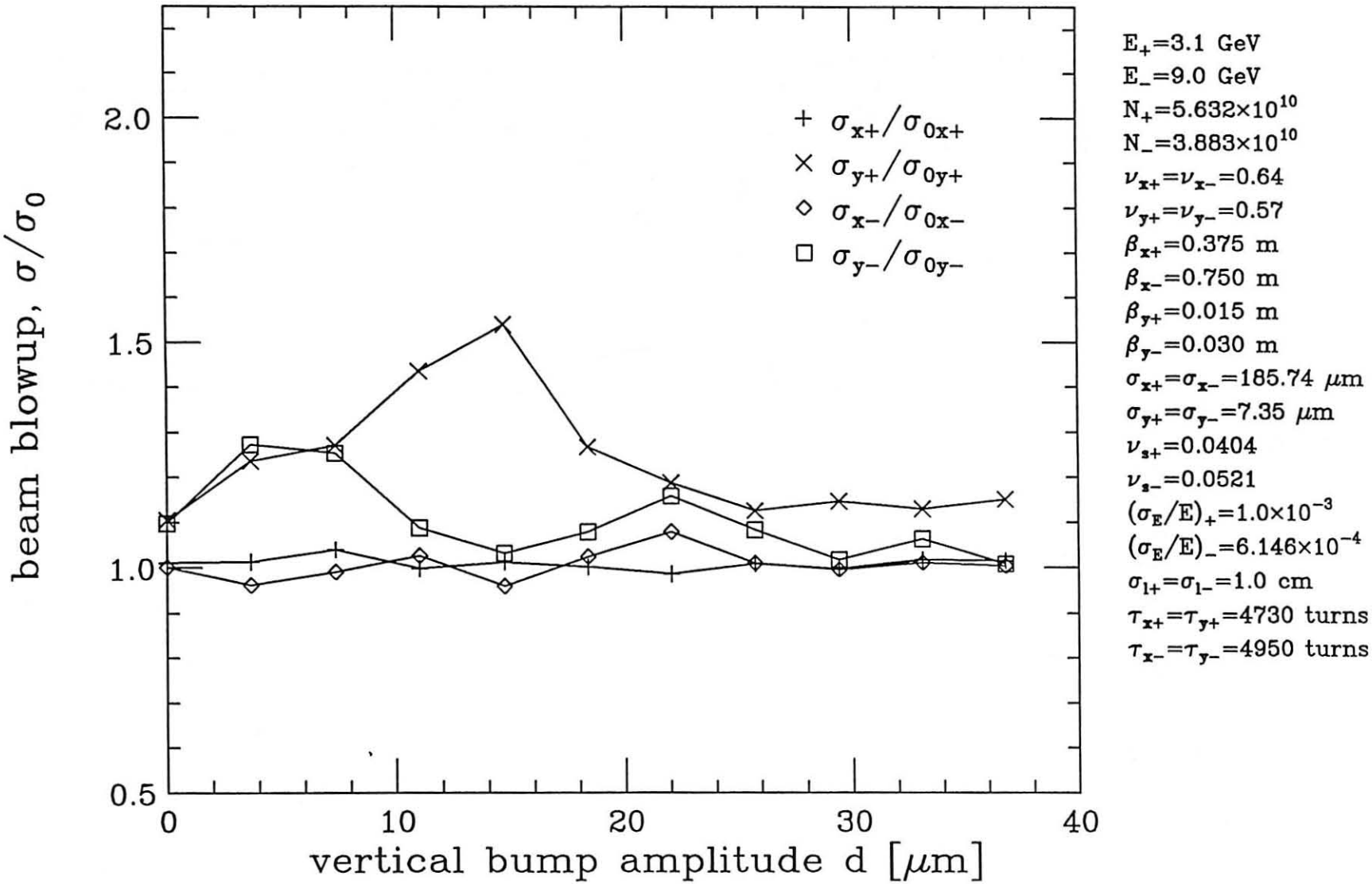

Fig. 13. Beam blowup relative to nominal beam size (Yokoya's code). Details of the simulation are explained in Sec. 4.

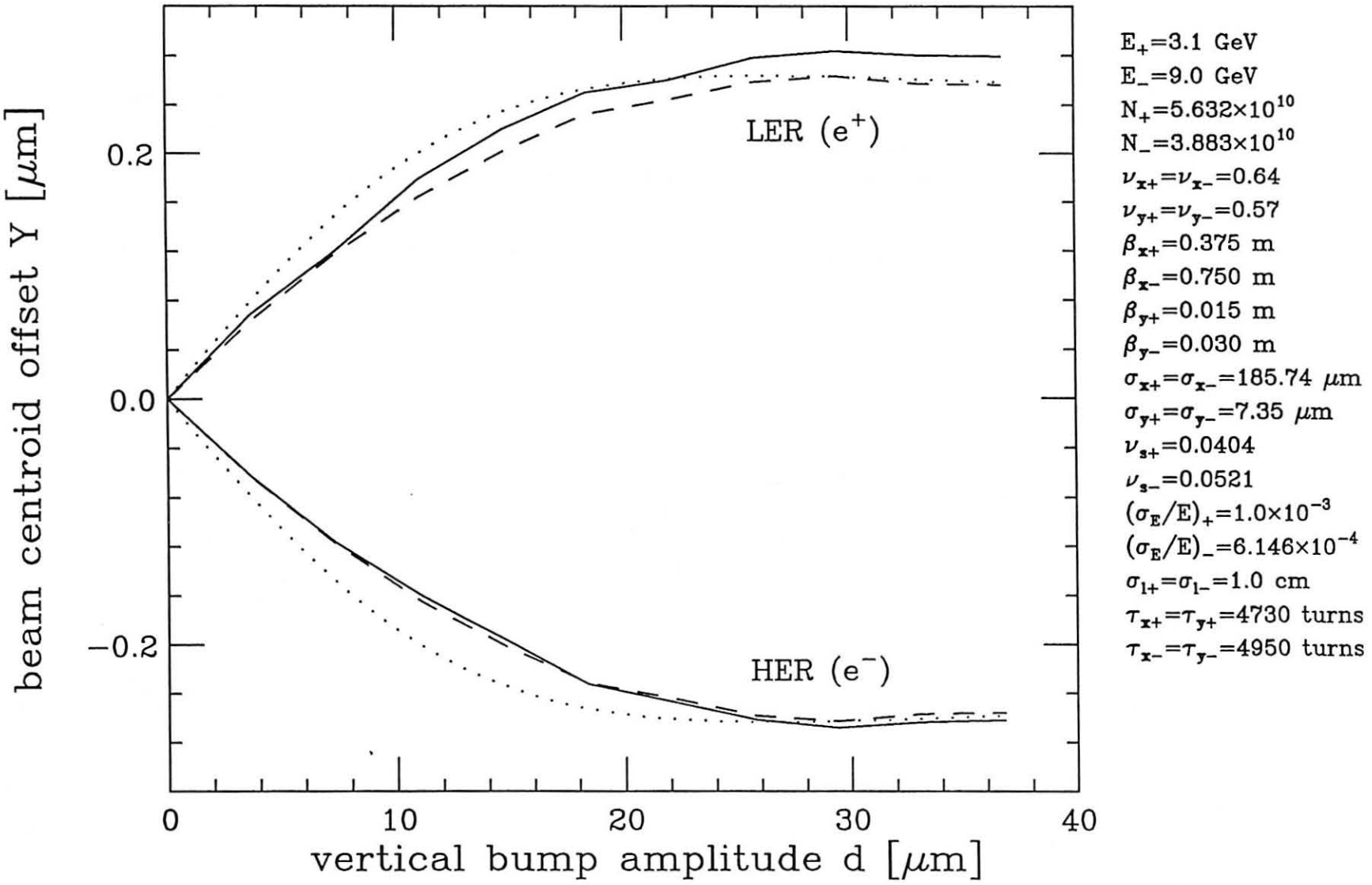

Fig. 14. Dependence of beam centroid offset on bump amplitude. The three sets of curves correspond to the full simulation using Yokoya's code (solid), the analytical result from Eq. (2.10) using nominal beam sizes (dotted), and the analytical result from Eq. (2.10) but using blown up beam sizes (dashed) as obtained from the full simulation and shown in Fig. 13.

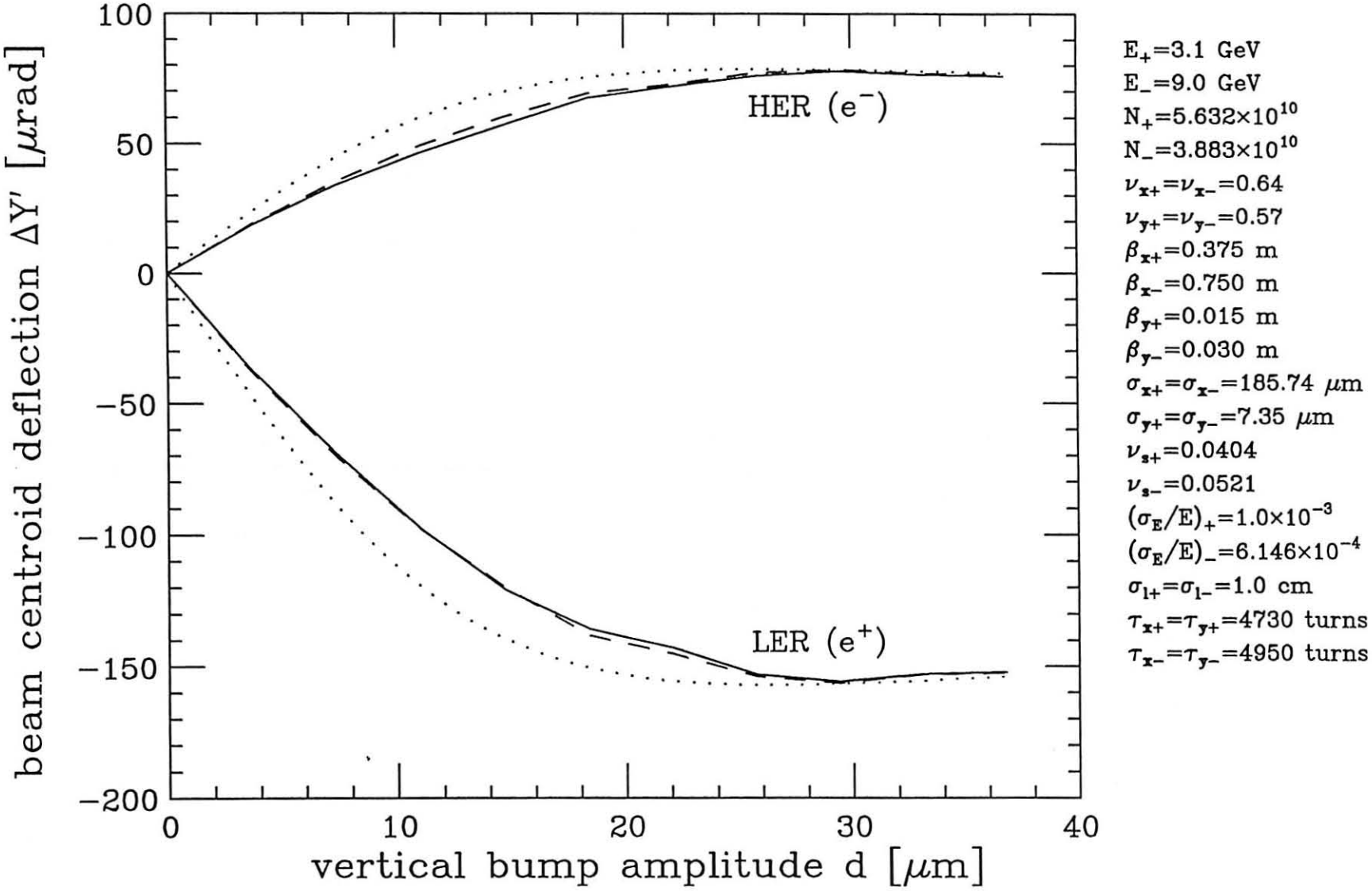

Fig. 15. Dependence of beam centroid deflection on bump amplitude. The three sets of curves parallel those in Fig. 14 (Yokoya's code).

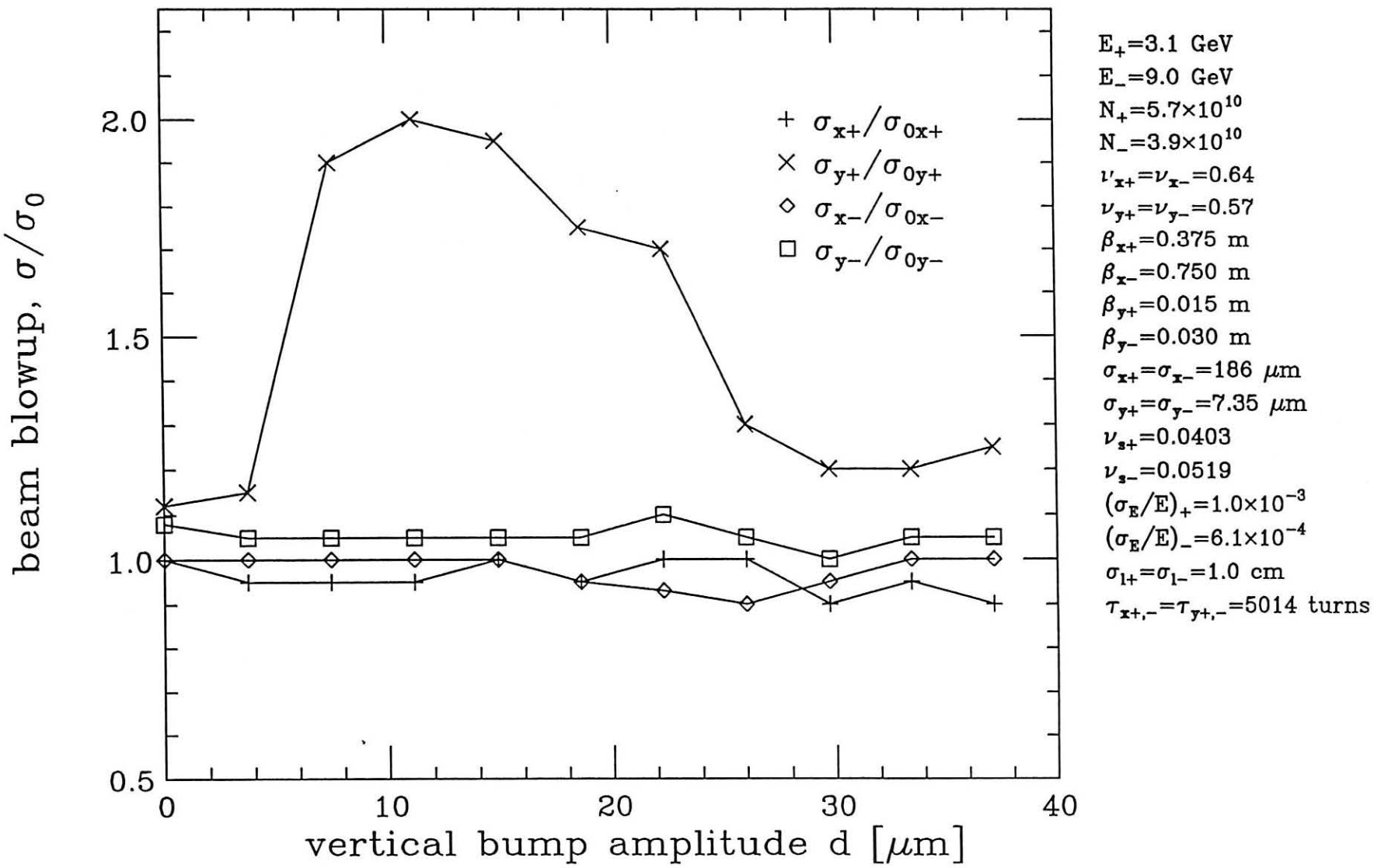

Fig. 16. Beam blowup relative to nominal size (Tennyson's code).

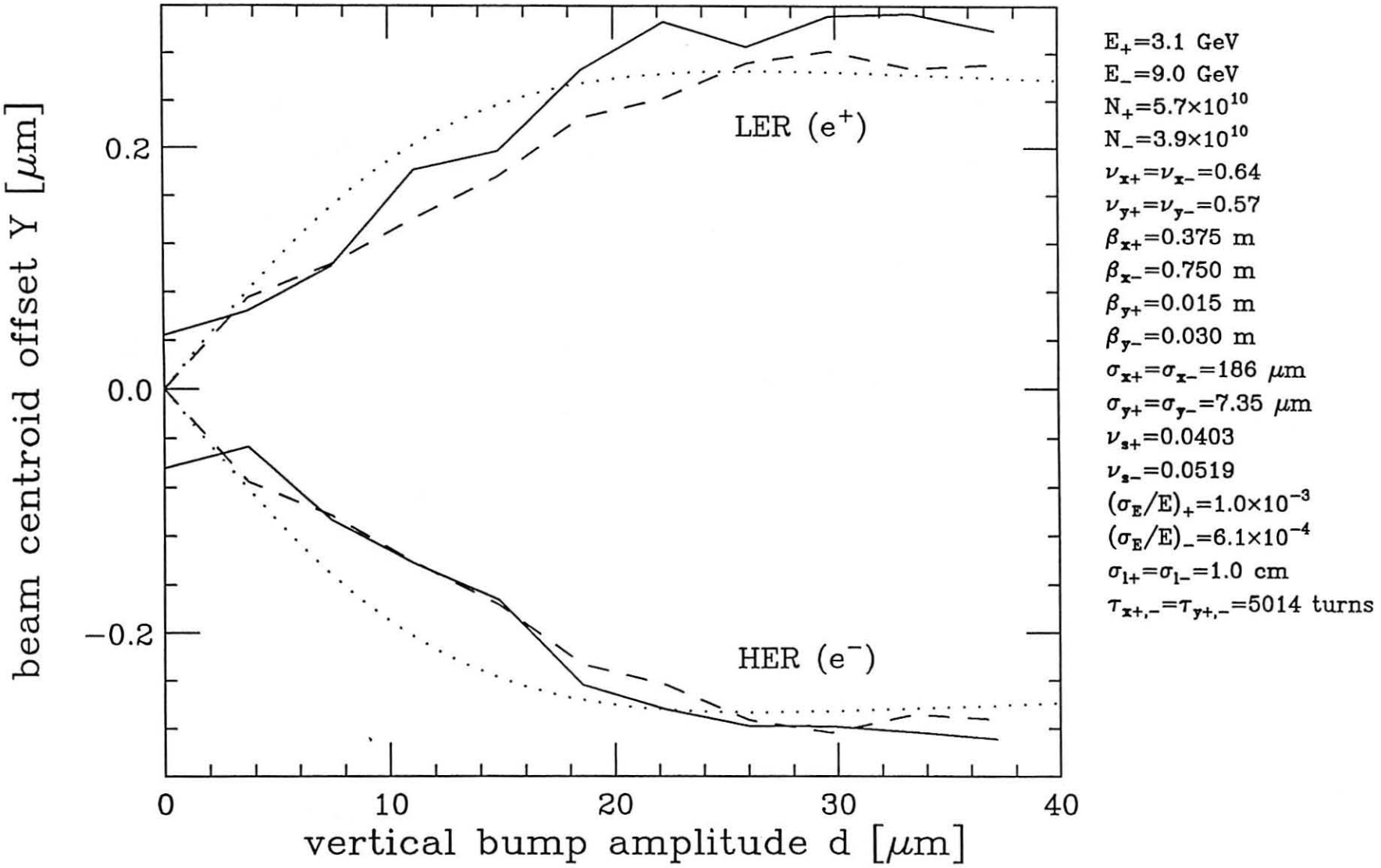

Fig. 17. Dependence of beam centroid offset on bump amplitude. The three sets of curves correspond to the full simulation using Tennyson's code (solid), the analytical result from Eq. (2.10) using nominal beam sizes (dotted), and the analytical result from Eq. (2.10) but using the blown up beam sizes (dashed) shown in Fig. 16. The nonzero offset at d=0 is due to the statistical error affecting the centroid calculation, which uses a relatively coarse sampling; it is representative of the statistical fluctuations at all beam separations.

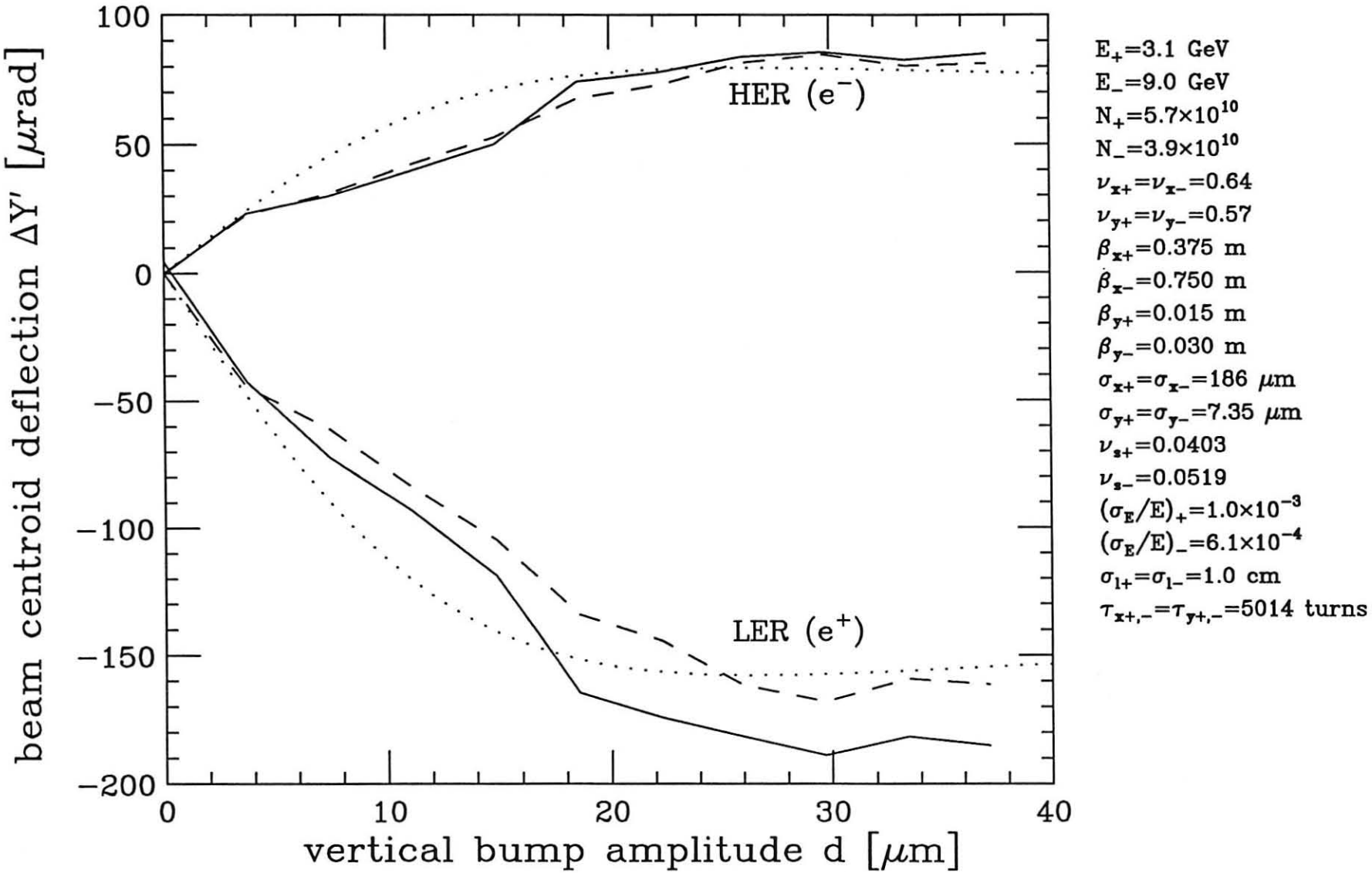

Fig. 18. Dependence of beam centroid deflection on bump amplitude. The three sets of curves parallel those in Fig. 17 (Tennyson's code).

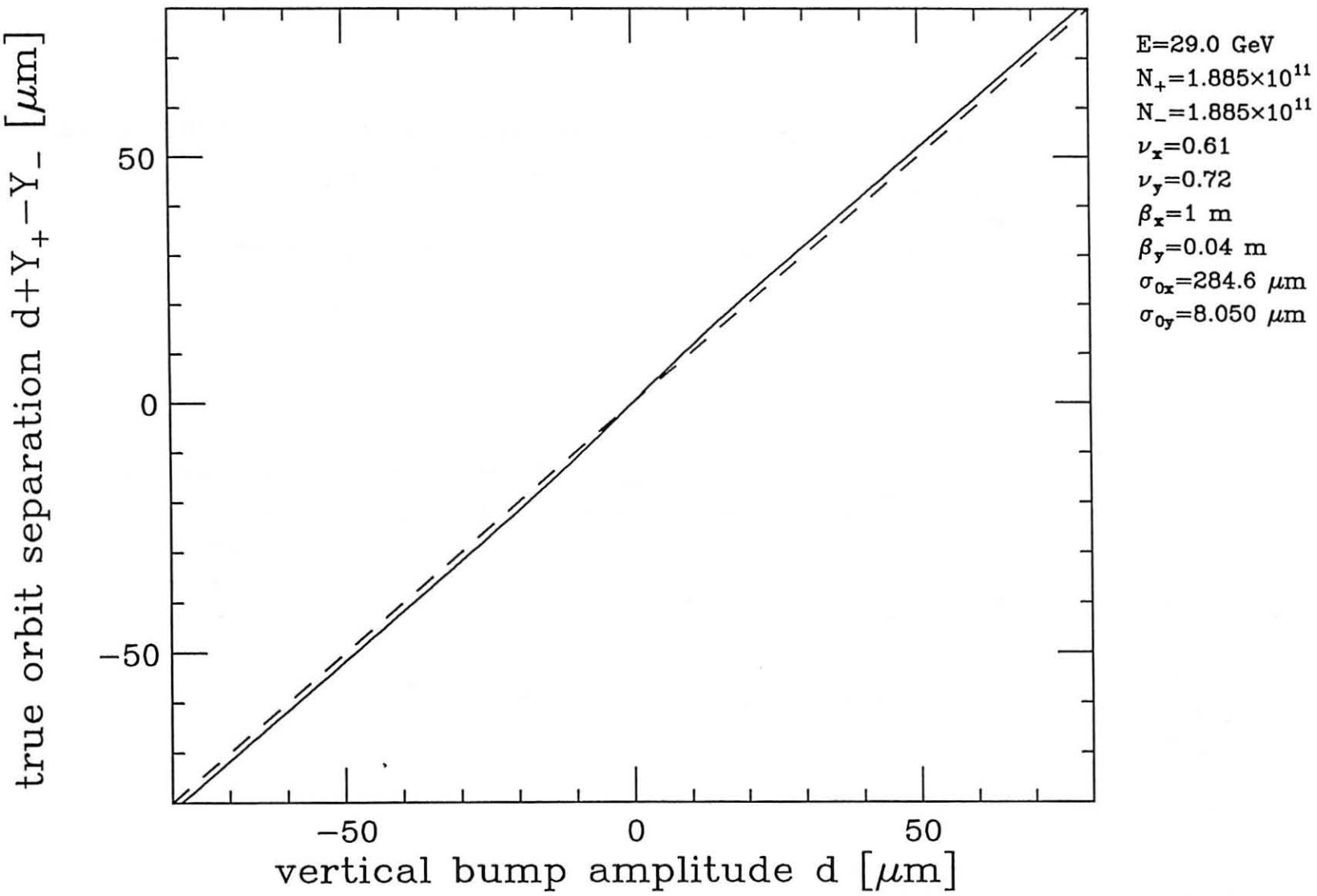

Fig. 19. True orbit separation at the IP (solid line) for TRISTAN. The dashed line is a straight line along the diagonal, for reference.

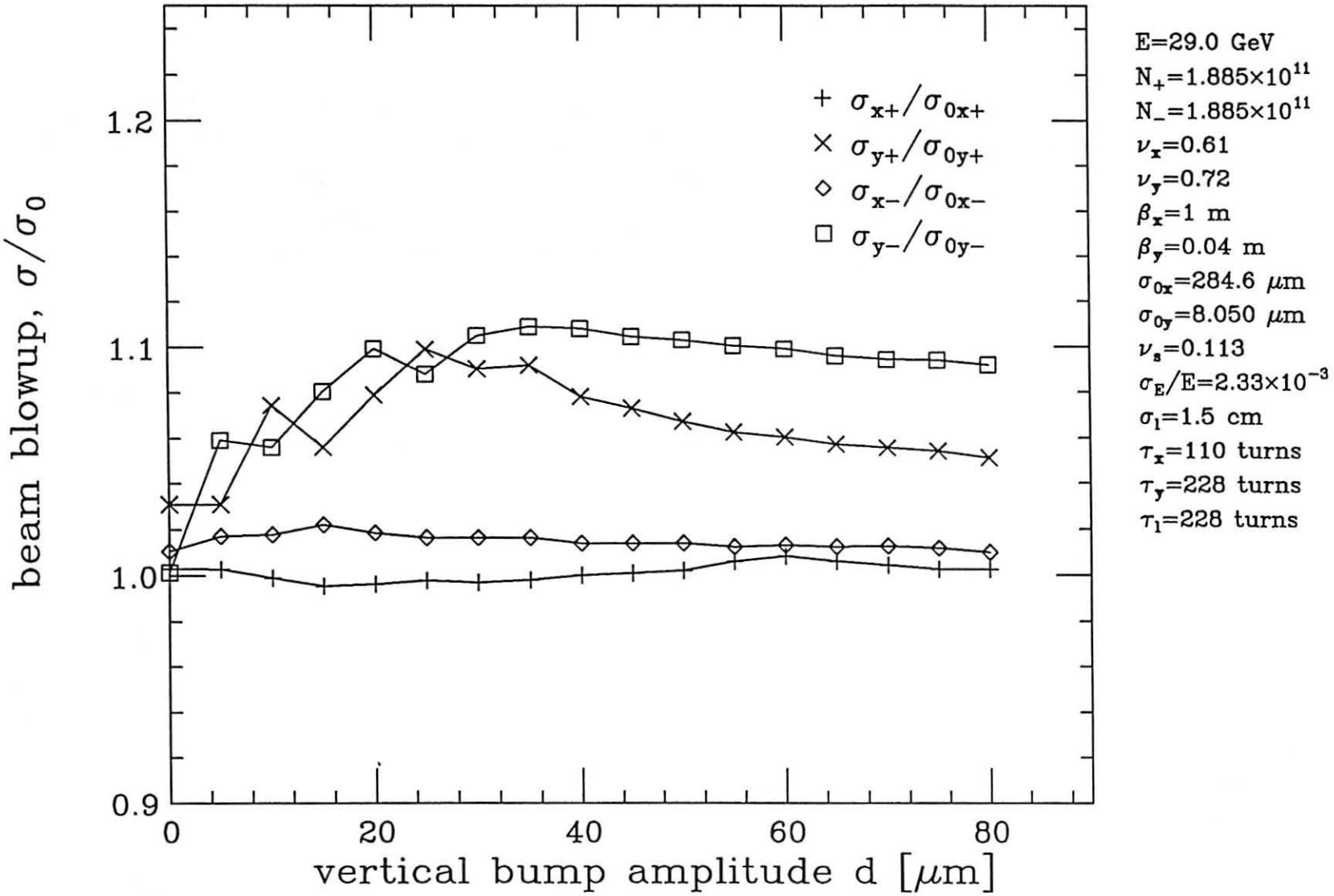

Fig. 20. Beam blowup relative to nominal beam size for TRISTAN (Yokoya's code).

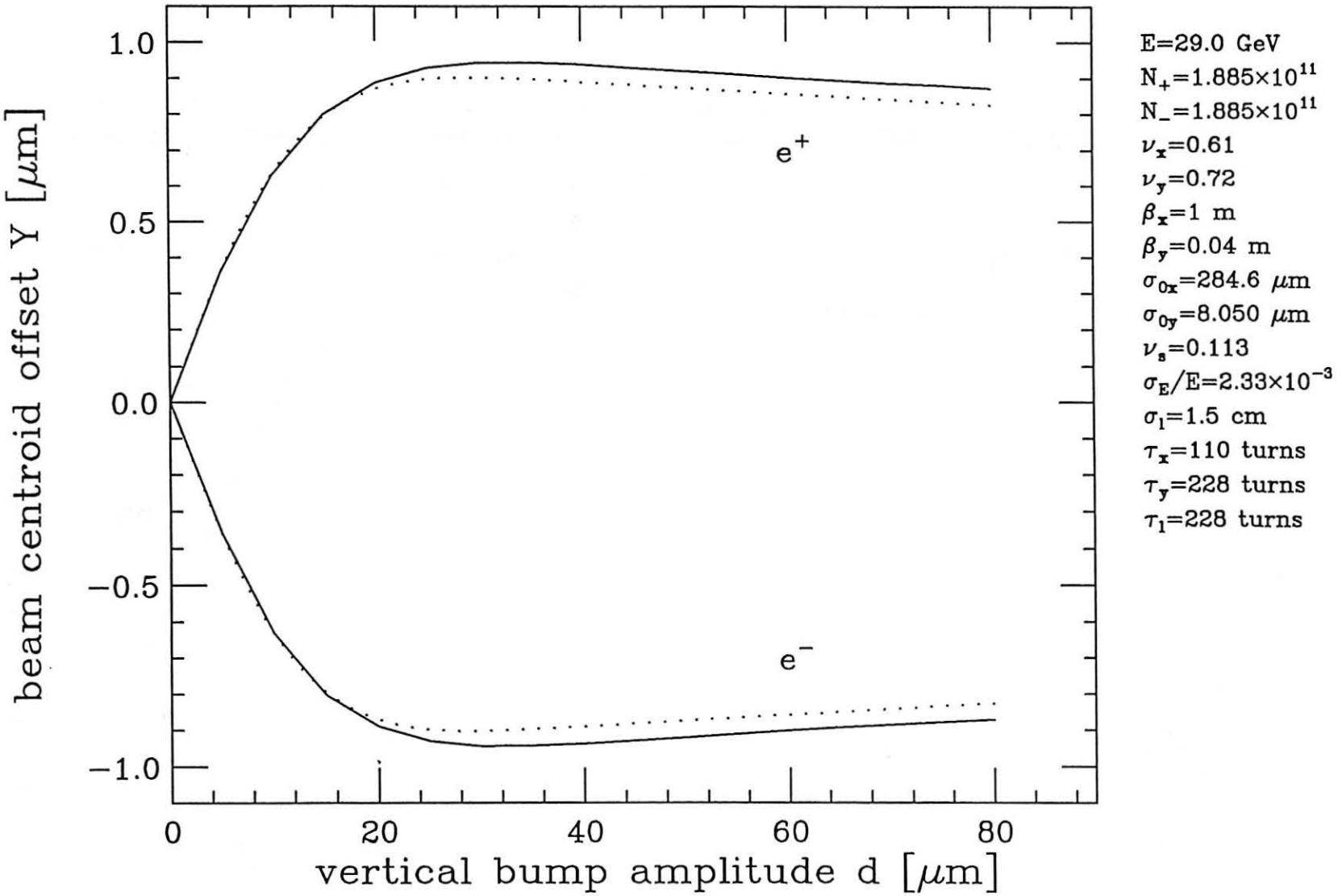

Fig. 21. Dependence of beam centroid offset on bump amplitude for TRISTAN. The two sets of curves correspond to the the full simulation using Yokoya's code (solid), and the analytical results from Eqs. (2.10) using the nominal beam sizes (dotted).

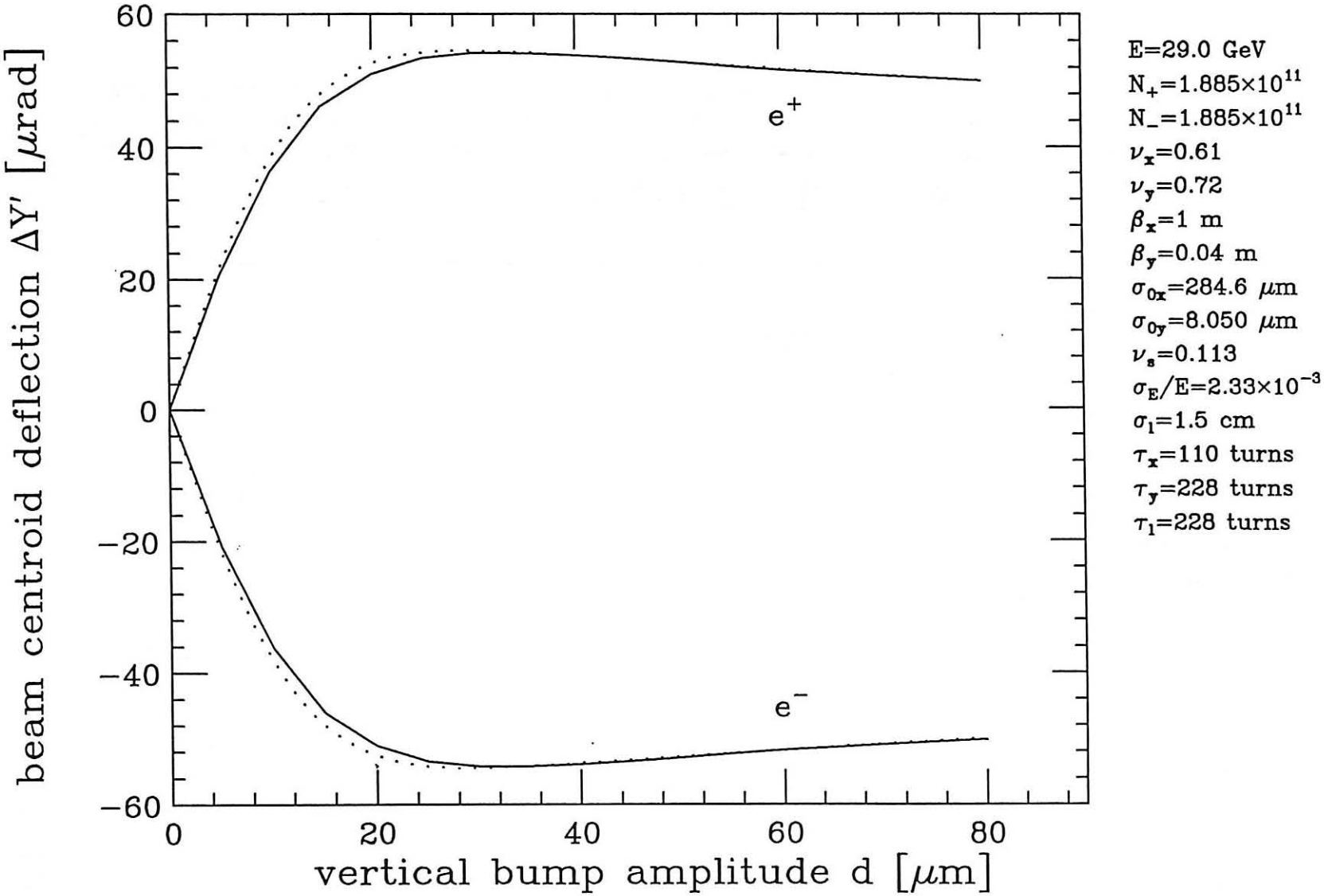

Fig. 22. Dependence of beam centroid deflection on bump amplitude for TRISTAN (Yokoya's code). The two sets of curves parallel those in Fig. 21.